

1 Input-adaptive linear mixed-effects model for estimating alveolar 2 Lung Deposited Surface Area (LDSA) using multipollutant datasets

3 Pak Lun Fung^{1,2}, Martha A. Zaidan^{1,2,3}, Jarkko V. Niemi⁴, Erkka Saukko⁵, Hilka Timonen⁶, Anu Kousa⁴,
4 Joel Kuula⁶, Topi Rönkkö⁷, Ari Karppinen⁶, Sasu Tarkoma⁸, Markku Kulmala^{1,3}, Tuukka Petäjä^{1,3} and
5 Tareq Hussein^{1,9}

6 ¹Institute for Atmospheric and Earth System Research / Physics, Faculty of Science, University of Helsinki, Finland

7 ²Helsinki Institute of Sustainability Science, Faculty of Science, University of Helsinki, Finland

8 ³Joint International Research Laboratory of Atmospheric and Earth System Sciences, School of Atmospheric Sciences, Nanjing
9 University, Nanjing 210023, China

10 ⁴Helsinki Region Environmental Services Authority (HSY), P.O. Box 100, FI-00066 Helsinki, Finland

11 ⁵Pegasor Ltd., FI-33100 Tampere, Finland

12 ⁶Atmospheric Composition Research, Finnish Meteorological Institute, FI-00560 Helsinki, Finland

13 ⁷Aerosol Physics Laboratory, Physics Unit, Tampere University, FI-33720 Tampere, Finland

14 ⁸Department of Computer Science, Faculty of Science, University of Helsinki, Finland

15 ⁹Department of Physics, the University of Jordan, Amman 11942, Jordan

16 Correspondence to: Pak Lun Fung (pak.fung@helsinki.fi), Tareq Hussein (tareq.hussein@helsinki.fi)

17 **Abstract.** Lung deposited surface area (LDSA) has been considered to be a better metric to explain nanoparticle toxicity
18 instead of the commonly used particulate mass concentration. LDSA concentrations can be obtained either by direct
19 measurements or by calculation based on the empirical lung deposition model and measurements of particle size distribution.
20 However, the LDSA or size distribution measurements are neither compulsory nor regulated by the government. As a result,
21 LDSA data are often scarce spatially and temporally. In light of this, we develop a novel statistical model, named input-
22 adaptive mixed-effects (IAME) model, to estimate LDSA based on other already existing measurements of air pollutant
23 variables and meteorological conditions. During the measurement period in 2017–2018, we retrieved LDSA data measured by
24 Pegasor AQ Urban and other variables at a street canyon (SC, average LDSA = $19.7 \pm 11.3 \mu\text{m}^2 \text{cm}^{-3}$) site and an urban
25 background (UB, average LDSA = $11.2 \pm 7.1 \mu\text{m}^2 \text{cm}^{-3}$) site in Helsinki, Finland. For the continuous estimation of LDSA, the
26 IAME model was automated to select the best combination of input variables, including a maximum of three fixed effect
27 variables and three time indicators as random effect variables. Altogether, 696 sub-models were generated and ranked by the
28 coefficient of determination (R^2), mean absolute error (MAE) and centred root-mean-square differences ($cRMSD$) in order. At
29 the SC site, the LDSA concentrations were best estimated by mass concentration of particle of diameters smaller than $2.5 \mu\text{m}$
30 ($PM_{2.5}$), total particle number concentration (PNC) and black carbon (BC), all of which are closely connected with the vehicular
31 emissions. At the UB site the LDSA concentrations were found to be correlated with $PM_{2.5}$, BC and carbon monoxide (CO).
32 The accuracy of the overall model was better at the SC site ($R^2 = 0.80$, $MAE = 3.7 \mu\text{m}^2 \text{cm}^{-3}$) than at the UB site ($R^2 = 0.77$,
33 $MAE = 2.3 \mu\text{m}^2 \text{cm}^{-3}$) plausibly because the LDSA source was more tightly controlled by the close-by vehicular emission
34 source. The results also demonstrated d that the additional adjustment by taking random effects into account improved s the
35 sensitivity and the accuracy of the fixed effect model. Due to its adaptive input selection and inclusion of random effects,
36 IAME could fill up missing data or even serve as a network of virtual sensors to complement the measurements at reference
37 stations.

38 1 Introduction

39 Particulate matter is one of the key components determining urban air pollution. Particulate matter can be described by a
40 combination of varying concentration (number, surface area and mass) and chemical composition. The mass concentrations of
41 particulate matter are dominated by large particles whereas the number concentrations are governed by sub-micron particles
42 (particle diameter (d_p) $< 1 \mu\text{m}$), particularly ultrafine particles (UFP, $d_p < 0.1 \mu\text{m}$) (e.g. Petäjä et al., 2007; Rönkkö et al., 2017;

43 Zhou et al., 2020). Particulate matter of varying sizes, carrying various harmful substances, have been known for playing a
44 major role in adverse health effects (Dockery et al., 1993; Oberdorster, 2012; Shiraiwa et al., 2017) in particular to respiratory
45 systems. A particle could be deposited in lung airways upon inhalation (Oberdörster et al., 2005) through three main
46 mechanisms: inertial impaction, gravitational sedimentation and Brownian diffusion. ~~Interception, and electrostatic forces are~~
47 ~~to a lesser extent.~~ An airborne particle might be inhaled either through nasal or oral passage and enter the respiratory tract.
48 Coarser particles (~~5–30 µm~~) are usually partly deposited in the head airway by the inertial impaction mechanism because they
49 cannot follow the air streamline. Some finer particles (~~1–5 µm~~) are deposited in the tracheobronchial region, mainly through
50 gravitational sedimentation while some are removed by mucociliary clearance (Gupta and Xie, 2018). The remaining sub-
51 micron particles diffuse by Brownian motion and penetrate deeply into the alveolar region, which is considered to be the most
52 vulnerable section in lungs because removal mechanisms might be insufficient (Gupta and Xie, 2018). The surface area of
53 inhaled particulate matter could also function as a carrier, or act as a transport vector, for many bacteria and viruses, including
54 the SARS-CoV-2 virus (COVID-19, Prather et al., 2020), which is responsible for the pandemic recently declared by the World
55 Health Organization (WHO). Particulate matter may, therefore, increase the effectiveness of the virus spread in the aerosol as
56 it creates a microenvironment suitable for its persistence (Liu et al., 2018a). ~~Regular exposure to particulate matter increases~~
57 ~~the chance to suffer from acute and chronic diseases (Brown et al., 2001; Oberdörster et al., 2005), and the susceptibility and~~
58 ~~severity of the COVID-19 patients' symptoms (Fennelly, 2020). In light of this and therefore,~~ besides commonly monitored
59 particulate matter number concentration and mass concentration, the surface area of a particle is also an important factor when
60 considering the harmfulness of particulate matter (Duffin et al., 2002). In particular, the total surface area of particles which
61 are deposited in alveolar section of human lungs, known as Lung Deposited Surface Area (LDSA), is of the greatest concern
62 because in vitro nanoparticle toxicity has been demonstrated to be better explained when the lung burden was expressed as
63 total particle surface area instead of atmospheric particulate matter mass (e.g. Brown et al., 2001; Oberdorster, 2012; Schmid
64 and Stoeger, 2016).

65
66 LDSA can be considered as an intermediary parameter between particle mass and particle number concentration as it cannot
67 be simply inferred from either of those parameters. Moreover, due to the various deposition efficiency with respect to particle
68 sizes, the quantification of LDSA is not simple. Conventionally, LDSA concentrations can be retrieved by (1) derivation from
69 particle size distribution with a deposition model or (2) direct measurements.

70
71 By fitting experimental lung deposition data on human beings, empirical deposition models are developed with the use of the
72 lung deposition model modified by Yeh and Schum (1980). Examples include the International Commission on Radiological
73 Protection (ICRP) Human Respiratory Tract Model (ICRP, 1994), the NCRP model (NCRP, 1997) and Multiple Path Particle
74 Dosimetry (MPPD) model (Anjilvel and Asgharian, 1995). Different conceptual particle deposition models vary primarily
75 with respect to lung morphometry and mathematical modelling techniques, rather than by using different deposition equations.
76 The three whole lung deposition models define regions of the human lungs (head airway, tracheobronchial and alveolar) for
77 any combination of particle size and breathing pattern (Hofmann, 2009). Among all models, single-path models, such as ICRP
78 model, are often used over multiple-path models due to their simplicity and their applicability to an average path without
79 requiring detailed knowledge of the branching structure of lungs. Owing to a higher potential health risk, LDSA in alveolar
80 region is often of greatest concern and it can be calculated by summing up the products of the surface concentration across
81 particle size spectrum and their corresponding deposition efficiency based on the selected deposition model.

82
83 Apart from numerical computation method, LDSA could also be measured by accredited instruments. ~~LDSA concentration in~~
84 ~~many urban environments is mainly driven by the particles smaller than 400 nm (Asbach et al., 2009; Kuuluvainen et al.,~~
85 ~~2016), generated vastly by anthropogenic sources such as vehicular exhaust emissions (Karjalainen et al., 2016) and residential~~

86 wood combustion (Tissari, 2008) which typically produce large amount of small particles. The impact of larger particles (>400
87 nm) might be significant due to regional background in very polluted cities (e.g. Delhi, Salo et al., 2021a; Salo et al., 2021b)
88 or very low quality residential burning in detached housing areas (e.g. HMA, Pirjola et al., 2017). These small particles cannot
89 be measured precisely with methods relying solely on optical detection (e.g. no artificial growing of particles) as the light
90 scattering intensity of these particles is weak (Kulkarni et al., 2011). Hence alternative approaches are required. One approach
91 is filter sampling of aerosolised material followed by gas adsorption method (e.g. Lebouf et al., 2011). Another more common
92 approach is using a diffusion charging based technique is a common approach where particles are charged with a unipolar
93 corona charger (Fissan et al., 2006). This method enables measurement of ultrafine particles and, more specifically, the LDSA
94 concentration with good accuracy (Todea et al., 2015) and stable performance in long term measurements (Rostedt et al.,
95 2014). Nanoparticle Surface Area Monitor (NSAM) has been used for decades (e.g. Asbach et al., 2009; Hama et al., 2017;
96 Kiriya et al., 2017; Hennig et al., 2018), and several other instruments and sensors, including DiSCmini, Testo Inc. (e.g. Eeftens
97 et al., 2016; Habre et al., 2018) and Partector, Naneos Ltd. (e.g. Cheristanidis et al., 2020), and Pegasor AQ Urban, Pegasor
98 Ltd. (e.g. Kuuluvainen et al., 2018; Kuula et al., 2020), using similar measuring techniques, are developed later on. ~~Recently,~~
99 ~~this diffusion charging based LDSA measurement has been combined with electrical cascade impactor method, which enables~~
100 ~~high time resolution measurements of particle LDSA size distributions (Lepistö et al., 2020).~~ Using these instruments in
101 campaigns and continuous measurements, LDSA concentrations in alveolar region and size distribution measurements in
102 various environments have been reported across the globe in the past decade (~~Table 1~~Table 4). When comparing LDSA
103 concentrations measured by different instruments, ~~it should be noted that~~ the instruments' limitations should be ~~taken into~~
104 ~~account~~considered in experimental LDSA studies, which will be further discussion in Sect. 2.2.

105
106 Although each of these methods is capable of measuring aerosol surface area concentrations, the corresponding uncertainties
107 (~~Asbach et al., 2017~~) and cost hinder the widespread use in monitoring networks (Asbach et al., 2017). Even though the
108 instruments are available, missing data often takes place due to instruments maintenance and data corruption. Kuula et al.
109 (2020) demonstrated high correlations of measured LDSA concentrations with black carbon (BC) and nitrogen oxide (NO_x)
110 ~~in traffic environments, under certain circumstances.~~ Traffic activities have been observed to be significant source contribution
111 to the LDSA concentrations (Järvinen et al., 2015). A clear correlation was also found between the emission factors of exhaust
112 plume BC and LDSA in on-road studies for city buses (e.g. Järvinen et al., 2019). These highly correlating relationships
113 provide good grounds for estimating LDSA concentrations and short-term trends by the other pollutants measured at the same
114 site with the use of data mining-based approach as statistical models. These statistical models can eventually turn into virtual
115 sensors of LDSA after being validated even under the circumstances of no actual instrumental LDSA measurements. Due to
116 the health effects LDSA has demonstrated, it is of great importance to researchers that continuous measurements of LDSA are
117 available with the help of these virtual sensors via statistical models. Similar approach for sensor virtualisation of BC
118 measurement has been studied in Fung et al. (2020).

119
120 Data mining-based approach exploits statistical or machine learning techniques to detect patterns between predictors and
121 dependent variables in the time series data. They do not demand in-depth understanding of air pollutant dynamics, but
122 evaluation by experts is still required to determine whether the models work properly. Simple yet apprehensible models, such
123 as multiple linear regression (MLR, e.g. Fernández-Guisuraga et al., 2016) and generalized additive models (GAM, e.g. Chen
124 et al., 2019), are commonly utilised as white-box models in air pollutant proxy studies. Furthermore, more sophisticated
125 machine learning black-box models, such as artificial neural network (ANN, e.g. Cabaneros et al., 2019; Zaidan et al., 2019;
126 Fung et al., 2021a), nonlinear autoregressive network with exogenous inputs (NARX, e.g. Zaidan et al., 2020) and support
127 vector regression (SVR, e.g. Fung et al., 2021b), have been intensively investigated in recent years. They work better in terms

128 of accuracy; however, they provide limited transparency and accountability regarding the outcomes (Rudin, 2019; Fung et al.,
129 2021b).

130

131 Apart from model structures, the criteria of selecting variables in multipollutant datasets for model development have received
132 considerable attention over the years, and a large number of methods have been proposed (Miller, 2002). Traditional methods,
133 like stepwise procedures, which is a combination of forward selection and backward elimination (e.g. Liu et al., 2018b; Chen
134 et al., 2019), can be unstable because it uses restricted search through the space of potential models, which eventually causes
135 inherent problem of multiple hypothesis testing (Breiman, 1996; Faraway, 2014). Another approach named regularization has
136 emerged as a successful method to reduce the data dimension in an automated way, yet deal poorly with multi-collinear
137 variables, for example Least Absolute Shrinkage and Selection Operator (LASSO, e.g. Fung et al., 2021b; Šimić et al., 2020),
138 ridge regression (e.g. Chen et al., 2019) and ELASTINET (e.g. Chen et al., 2019). Criterion-based procedures, which choose
139 the best predictor variables according to some criteria (e.g. coefficient of determination, residual, etc), are sensitive to outliers
140 and influential points, but involve a wider search and compare models in a preferable manner. Examples are best subset
141 regression (e.g. Chen et al., 2019), input adaptive proxy (IAP, e.g. Fung et al., 2020; Fung et al., 2021b), etc. Hastie et al.
142 (2020) compared some of the models using the three approaches and concluded that no single feature selection method
143 uniformly outweighs the others. Despite the extensive research of feature selection methods, the inclusion of random effects
144 together with the fixed effects as linear mixed-effects (LME) model has received relatively little attention (e.g. Mikkonen et
145 al., 2020; Tong et al., 2020) in air pollution research, let alone LDSA study in particular. This inclusion of random effects
146 could acknowledge a possible effect coming from a factor where specific and fixed values are not of interest.

147

148 In this study, we combine the use of criterion-based feature selection method and the inclusion of random effects, and develop
149 a novel input-adaptive mixed effects (IAME) model to estimate alveolar LDSA concentrations, which is the first study of this
150 context to our best knowledge. The description of LDSA measurements and the techniques of IAME model are outlined in
151 Sect. 2 and 3, respectively. Section 4 presents the characteristics of alveolar LDSA, including its seasonal variability, weekend
152 effect and diurnal pattern, in four types of environments. We also aim to investigate the correlation with other air pollutants.
153 In Sect. 5, we evaluate the performance of the IAME proxy ($LDSA_{IAME}$) with the measured alveolar LDSA by Pegasor AQ
154 Urban ($LDSA_{Pegasor}$), ICRP lung deposition model derived LDSA ($LDSA_{ICRP}$) and another modelled alveolar LDSA by IAP
155 ($LDSA_{IAP}$) as well as the benefits and implication of this alveolar LDSA model as virtual sensors. It should be noted that this
156 study discusses LDSA in alveolar region, unless stated otherwise.

157 **2 Measurement description**

158 **2.1 Measurement sites**

159 We retrieved aerosol, gaseous and meteorological data from two types of measurement sites, i.e., street canyon (SC, 2017–
160 2018) and urban background (UB, 2017–May 2018), in Helsinki Metropolitan Area (HMA) described in more details s below.
161 Data from detached housing (DH, 2017) and regional background (RB, 2017) sites were also included in the study to provide
162 comparison and data from the background concentrations. Situated on a relatively flat land at the coast of Gulf of Finland,
163 HMA has land area of 715 km² and population of about 1.13 million inhabitants. Helsinki can be classified as continental or
164 marine climate depending on the air flows and the pressure system. Figure S1 and Table S1 show the detailed site description.
165 **Street canyon site (SC):** Mäkelänkatu urban supersite is operated by the Helsinki Region Environmental Services Authority
166 (HSY, Kuuluvainen et al., 2018). The station is located at 3 km from the city centre in a street canyon in the immediate vicinity
167 to one of the main roads leading to downtown Helsinki. The street, with speed limit of 50 km h⁻¹, consists of six lanes and two
168 tramlines. The annual mean traffic volume in 2018 per workday was 28 100 vehicles, 11% of which were recorded as the

169 heavy duty vehicles. The traffic loads are especially high during rush hours at 8 a.m. and 5 p.m. (Figure S2). The street canyon
170 of width of 42 m is surrounded by rows of buildings of 17 m high, which weaken the dispersion process of the direct vehicular
171 emissions. All the inlets for the measuring devices are positioned approximately at a height of 4 m from the ground level.

172 **Urban background site (UB):** The Station for Measuring Ecosystem-Atmosphere Relations III (SMEAR III, Järvi et al.,
173 2009) in Kumpula, situated on a rocky hill at 26 m above sea level, is about 4 km northeast from the Helsinki centre. The
174 surroundings of this urban background station are heterogeneous, constituting of residential buildings, small roads, parking
175 lots, patchy forest and low vegetation from different direction. One main road (45 000 vehicles per workday) is located at the
176 distance of 150 m east from the site. Trace gases and meteorological conditions are measured at a height of 4 m and 32 m,
177 respectively, at a triangular lattice tower while aerosol measurements are conducted inside a container approximately 4 m
178 above the ground. The site is co-operated by Finnish Meteorological Institute (FMI) and the University of Helsinki (UHEL).

179 **Detached housing site (DH):** Three measurement stations, Rekola (DH1), Itä-Hakkila (DH2) and Hiekkaharju (DH3), were
180 chosen since they represent a sub-urban residential area surrounded by detached houses. These sites are mainly affected by the
181 wood combustion emissions from residential activities, especially in cold weather conditions. Emissions from traffic source
182 also account for a small portion of the whole pollution. It is estimated that 90 % of the households burn wood to warm up
183 houses and saunas, less than 2 % of which use wood burning as the main heating source in detached houses in HMA (Hellén
184 et al., 2017).

185 **Regional background site (RB):** The RB site is located about 23 km away from the Helsinki city centre at Luukki, surrounded
186 by a wooded outdoor recreational area right at the edge of the Greater Helsinki golf course. The measuring station is in an
187 open place away from busy traffic routes and large point sources. As a result, this site can represent background concentration
188 levels outside the urban area without any main local sources.

189 2.2 Instruments

190 **LDSA measurements:** The sensor unit and the core of the Pegasor AQ Urban is practically another instrument called a Pegasor
191 PPS-M sensor (Pegasor Ltd., Finland) originally designed for automotive exhaust emission measurements (e.g. Maricq, 2013;
192 Amanatidis et al., 2017). The operation of the sensor is based on diffusion charging of particles and the measurement of electric
193 current without the collection of particles. The diffusion charging of particles is carried out by a corona-ionized flow that is
194 mixed with the ambient sample air in an ejector diluter inside the sensor. The sampling lines and the sensor unit are heated to
195 40°C above the ambient temperature (1) to dry the aerosol sample, (2) to prevent interference from humidity, and (3) to prevent
196 any water condensation inside the sensor. The performance of the Pegasor PPS-M sensors for long-term ambient measurements
197 has been improved after they were tested in Helsinki (Järvinen et al., 2015) and Beijing (Dal Maso et al., 2016). The suggestions
198 have been considered for the design of the current form of the Pegasor AQ Urban in this study.

199 The Pegasor AQ Urban (dimension: 320 mm×250 mm×1000 mm), which consists of a weatherproof cover, clean air supply,
200 and the abovementioned Pegasor PPS-M sensor, has been designed such that its response to LDSA is not to be subjected to
201 meteorological fluctuation for outdoor operation. Kuuluvainen et al. (2016) used two Pegasor AQ Urban devices during a 2
202 week period at an urban street canyon and an urban background measurement station in Helsinki, Finland whereas Kuula et
203 al. (2019) later used the instruments in a 3 month long campaign at the same urban street canyon station. These studies
204 demonstrated that the output signal of the Pegasor AQ Urban correlated well with other devices measuring LDSA
205 concentrations such as the Partector and DiSCmini. Kuula et al. (2020) further validated the accuracy and stability of Pegasor
206 AQ Urban at the street canyon station by comparing the measured values of one full year with DMPS reference instruments
207 ($R^2R^2 = 0.90$, $RMSERMSE = 4.1 \mu\text{m}^2 \text{cm}^{-3}$). The internal precision of Pegasor AQ Urban is $\pm 3\%$, but this was not tested
208 prior the campaignKuula et al., 2020. The instrument is optimized to measure the alveolar LDSA concentrations of particles
209 in ~10–400 nm size range. Pegasor AQ Urban tends to underestimate LDSA of particle larger than about 400 nm. In typical
210 urban environments, most of the particles from local combustion sources are in the size below the threshold (Asbach et al.,

211 2009; Kuuluvainen et al., 2016; Pirjola et al., 2017), generated vastly by anthropogenic sources such as vehicular exhaust
212 emissions (Karjalainen et al., 2016) and residential wood combustion (Tissari, 2008) which typically produce large amount of
213 small particles. However, the impact of larger particles (>400 nm) to alveolar LDSA might be significant, for example ~~a recent~~
214 ~~study on LDSA concentrations in polluted urban environment in India observed high LDSA contribution from relatively large~~
215 ~~accumulation mode particles although the experiment was conducted in close proximity of traffic (Salo et al., 2021a) and in~~
216 ~~mining environment the mineral dust and other pollutants being typically in larger particle sizes can also contribute to the~~
217 ~~LDSA concentrations (Salo et al., 2021b).~~ In HMA, ~~the impact of >400 nm might also be significant~~ during PM_{2.5} long-range
218 transport episodes or when there are many particles from very low-quality residential burning in detached housing areas
219 (Pirjola et al., 2017). The regional background source in very polluted regions (e.g. Delhi, Salo et al., 2021a; mining
220 environments, Salo et al., 2021b) could be another reason for the significant impact of larger particles. This limitation of
221 Pegasor AQ Urban should be considered when it comes to data analysis in Sect. 4 and 5.

222 **Aerosol measurements:** Differential mobility particle sizer (DMPS) in combination of a differential mobility analyser (DMA)
223 and a condensation particle counter (CPC) measures aerosol size distribution (Kulkarni et al., 2011). Vienna DMA and
224 Airmodus A20 CPC (measurements of particle size range 6–800 nm) ~~were~~ used at the SC site while a twin DMPS (Hauke-
225 type DMA and TSI Model 3025 CPC + Hauke-type DMA and TSI Model 3010 CPC, merged particle size range 3–1000 nm)
226 ~~were~~ used at the UB site. Both instruments make use of the bipolar charging of aerosol particles, followed by classification
227 of particles into size classes according to their electrical equivalent mobility. In addition to particle size distribution, total
228 particle number concentration (PNC, in cm⁻³) ~~was~~ calculated by summation. Particle mass concentration of diameter less than
229 2.5 μm (PM_{2.5}, in μg m⁻³) and less than 10 μm (PM₁₀, in μg m⁻³) ~~were~~ measured continuously with ambient particulate
230 monitor TEOM 1405 at the SC site and TEOM 1405-D at the UB site. Black carbon (BC, in μg m⁻³) mass concentration ~~was~~
231 measured by a multi-angle absorption photometer (MAAP) Thermo Scientific 5012 with a PM₁ inlet. The measured absorbance
232 ~~was~~ converted to BC mass concentration by using a fixed 6.6 m² g⁻¹ mass absorption coefficient at wavelength of 637 nm.
233 PM_{2.5}, PM₁₀ and BC ~~were~~ recorded in μg m⁻³.

234 **Ancillary measurements:** Trace gas concentrations (in ppb), including nitric oxide (NO), nitrogen dioxide (NO₂), their
235 sum nitrogen oxide (NO_x), ozone (O₃) and carbon monoxide (CO) ~~were~~ determined with a suite of gas analysers. In addition,
236 supporting meteorological variables, including air temperature (Temp), relative humidity (RH), air pressure (P), wind speed
237 (WS), wind direction (WD) and photosynthetically active radiation (PAR), ~~were~~ measured at SC and UB. Figure S3 show
238 the meteorological conditions during the measurement period. A list of collected variables ~~collected~~ is shown in Table S2.

239 3. Method

240 3.1 Data pre-processing

241 The collected data was quality checked by the corresponding operating organisation, HSY, FMI and UHEL. No additional
242 pre-processing was done for general analysis. For proxy development, outliers due to potential measurement errors were
243 detected (SC: 0.73%; UB: 0.99% overall) by using the interquartile range (IQR) rule, which is applicable for non-Gaussian
244 distribution sample. We calculated the cut-off for outliers as 2 times the IQR, subtracted this cut-off from the 25th percentile
245 and added it to the 75th percentile to give the actual limits on the data. We applied a natural logarithm transformation to all the
246 skewed-distributed aerosol and trace gases measurements in order to keep the distribution of each parameter following a normal
247 distribution. Since wind direction is a circular variable, it is resolved into North-South (WD–N) and East-West (WD–E) vector
248 components by trigonometric functions.

249 3.2 Size-fractionated lung deposited surface area (LDSA_{ICRP})

250 Alveolar deposition fraction (DF_{AL}) as a function of particle size with the unit density is determined with the ICRP Human
251 Respiratory Tract Model by the following equation (ICRP, 1994):

$$DF_{AL} = \left(\frac{0.0155}{d_p} \right) \left(\exp \left(-0.416 (\ln d_p + 2.84)^2 \right) + 19.11 \exp \left(-0.482 (\ln d_p - 1.362)^2 \right) \right) \quad (1),$$

252 where d_p is the aerodynamic diameter (μm) of spherical particles with the unit density (1 g cm^{-3}). The equation is determined
253 in two parts with respect to the two different peaks in the deposition curve in Figure 1. The peak near the size of 20 nm can be
254 approximated to represent the Brownian deposition, whereas the peak between 1 μm and 2 μm represents the inertial
255 deposition. From the particle number size distribution, we calculated the particle surface area distribution assuming each
256 particle is monodisperse sphere of standard density at standard conditions. By Eq. (1), a deposition factor for each particle size
257 bin (26 size bins at SC and 49 at UB) were calculated. Size-fractionated LDSA was then computed by multiplying the surface
258 area concentration with DF_{AL} in the corresponding size class. Total LDSA calculated by the ICRP lung model (LDSA_{ICRP}) can
259 be obtained by summing up the all the size-fractionated LDSA values (Hinds, 1999). In this study, the alveolar LDSA_{ICRP} was
260 calculated based on DMPS measurements in SC and UB. Thus, while the alveolar LDSA measured by Pegasor (LDSA_{Pegasor})
261 represent the ~10–400 nm size range, the alveolar LDSA_{ICRP} represent 6–800 nm and 3–1000 nm size range in SC and UB,
262 respectively.

263 3.3 Novel Input-adaptive mixed-effects (IAME) model

264 Input-adaptive mixed-effects (IAME) model is a combination of input-adaptive proxy (IAP) and linear mixed-effects (LME)
265 model. IAP was first introduced by Fung et al. (2020) and has been demonstrated reliable and flexible to fill up missing values
266 by taking input variables adaptively with robust ordinary least square regression models. IAP has been able to estimate BC
267 concentration by other air quality indicators with a satisfactory performance in two different categorised urban environments,
268 street canyon (adjusted $R^2 = 0.86\text{--}0.94$) and urban background (adjusted $R^2 = 0.74\text{--}0.91$). Some models outperformed IAP in
269 accuracy performance, but its transparent model structure and ability to impute missing values still make it a preferred option
270 as a virtual sensor (Fung et al., 2021b).

271
272 In this study, we primarily stick to the strength to select input variables adaptively with the introduction of mixed effects. The
273 mixed effect approach is a generalization of the linear model that can incorporate both fixed (i.e. causing a main
274 effect/interaction) and random effects (i.e. causing variance/variability in responses), allowing the account of several sources
275 of variations (Chudnovsky et al., 2012). As seen in [Figure 2](#), we picked the direct air pollutant measurement from
276 the station (variables of high correlation: PM_{2.5}, BC and NO₂ and other supporting variables: PM₁₀, O₃, NO_x, NO, CO and
277 PNC) and meteorological data of higher correlation (Temp, RH, P, PAR, WS, WD–N, WD–E) as the fixed variables because
278 the air pollutants can indicate the sources of LDSA which largely come from combustion and meteorological data could
279 influence the dispersion and dilution of LDSA. They are the most direct factors to the fluctuation of LDSA concentrations.
280 Due to the strong seasonal variation, weekend effects and diurnal pattern in urban air pollutant concentrations (Fung et al.,
281 2020), the variance in responses might depend on the time indicators that are not the primary cause of the concentration
282 variability, but they indirectly alter human-induced activities, such as traffic amounts. To take them into account, we created
283 three time hierarchical sub-groups (12 months of year, 7 days of week and 24 hours of day) as the inputs of random effect
284 variables.

285
286 The regression equation of IAME is similar to the equation of IAP, except that IAME includes additional intercepts term for
287 random effects as below:

$$y_i = \beta_0 + \sum_{k=1}^p \beta_{ik} x_{ik} + \sum_{j=1}^q b_{ij} + e_i \quad (2),$$

288 where y_i is the i^{th} estimated LDSA concentration. The first term on the right β_0 indicates the fixed intercept of the equation.
 289 The second term represents the total contribution by the direct measurement of variable x as fixed effects with a slope β at
 290 each data point i . A maximum of three inputs from the total 16 fixed variables are selected to from 696 sub-models ([Figure](#)
 291 [2Figure-2](#)). The inputs for random effects are indicated by b as intercepts of the corresponding three hierarchical sub-groups.
 292 A Gaussian error term is indicated by e . The explanation of Eq. [\(2\),\(2\)](#), is visualised in [Figure 2Figure-2](#).

293

294 One of the assumptions of LME models is that the random effects, together with the error term, have the following prior
 295 distribution:

$$b \sim N(0, \sigma^2 D(\theta)) \quad (3),$$

296 where D is a q -by- q symmetric and positive semidefinite matrix, parameterized by a variance component vector θ , q is the
 297 number of variables in the random-effects term, and σ^2 is the observation error variance. We use an optimiser, restricted
 298 maximum likelihood, commonly known as ReML, with the value 1×10^{-6} as the relative tolerance on gradient of objective
 299 function and 1×10^{-12} as absolute tolerance on step size. The use of ReML over the conventional ML could produce unbiased
 300 estimates of variance and covariance parameters (Lindstrom and Bates, 1988).

301

302 After the sub-model formation, the dataset ~~wasis~~ randomly divided into five portions. 80% of the data ~~were~~ allocated for 4-
 303 fold cross validation to remove variance of accuracy. The results of all the folds ~~were~~ averaged and the sub-models ~~were~~
 304 ranked by several evaluation metrics, which ~~were~~ further demonstrated in [Figure 2Figure-2](#) and described in Sect. 3.4. Some
 305 of the sub-models ~~were~~ subject to rejection under two conditions: (1) strong multi-collinearity among the fixed parameters
 306 (variance inflation factor (VIF) ~~exceeding a threshold of~~ ≥ 5) and (2) violation of the normality assumption of residuals also
 307 known as heteroscedasticity (fail in Kolmogorov-Smirnov (K-S) test, $p < 0.05$). Based on the situation of missing data, the
 308 automatised IAME model ~~will-would~~ search for the best sub-model option from the ranking chart. Hence, each data point
 309 might be estimated differently depending on the available data. The number of data points being estimated by each sub-model
 310 ~~wais~~ reported to show their frequency of usage.

311 3.4 Evaluation metrics

312 In order to evaluate the model performance quantitatively, we used the following metrics:

$$R^2 = 1 - \frac{\sum_{i=1}^N (y_i - \hat{y}_i)^2}{\sum_{i=1}^N (y_i - \bar{y})^2} \quad (4),$$

$$MAE = \frac{1}{N} \sum_{i=1}^N |y_i - \hat{y}_i| \quad (5),$$

$$cRMSD = \sqrt{\frac{1}{N} \sum_{i=1}^N ((y_i - \bar{y}) - (\hat{y}_i - \tilde{y}))^2} \quad (6),$$

$$r = \frac{\sum_{i=1}^N (y_i - \bar{y})(\hat{y}_i - \tilde{y})}{\sqrt{\sum_{i=1}^N (y_i - \bar{y})^2} \sqrt{\sum_{i=1}^N (\hat{y}_i - \tilde{y})^2}} \quad (7),$$

$$NSD = \frac{SD_{predicted}}{SD_{reference}} = \frac{\sqrt{\frac{1}{N-1} \sum_{i=1}^N (\hat{y}_i - \tilde{y})^2}}{\sqrt{\frac{1}{N-1} \sum_{i=1}^N (y_i - \bar{y})^2}} = \sqrt{\frac{\sum_{i=1}^N (\hat{y}_i - \tilde{y})^2}{\sum_{i=1}^N (y_i - \bar{y})^2}} \quad (8),$$

313 where \hat{y}_i and \tilde{y}_i are i^{th} measured data point and estimated variable by the model, respectively. \bar{y} and \tilde{y} are the expected value
 314 of the measured and modelled dataset, respectively. N is the number of complete data input to the model. Coefficient of

315 determination (R^2) is a measure of how close the data lie to the fitted regression line. It, however, does not consider the biases
316 in the estimation. Therefore, we further validated the models with mean absolute error (MAE) and centred root-mean-square
317 differences ($cRMSD$), where MAE measures the arithmetic mean of the absolute differences between the members of each
318 pair, whilst $cRMSD$ calculates the square root of the average squared difference between the forecast and the observation pairs.
319 $cRMSD$ is more sensitive to larger errors than MAE . Furthermore, together with $cRMSD$, Pearson correlation coefficient (r)
320 and normalised standard deviation (NSD) of the modelled data set are also studied. r describes the correlation between the
321 measured and modelled data whereas NSD measures the relative spread of the data. Due to their unique mathematical
322 relationship, the three metrics can be portrayed on Taylor's diagram, which has been used for sub-model selection purpose.
323 We ranked our sub-models first by R^2 , followed by MAE and $cRMSD$. r and NSD serve as additional evidence when we
324 explain the model performance.

325 3.5 Two-sample t-tests

326 We assessed the temporal and spatial impact on the IAME model by comparing the means of absolute differences between the
327 hourly measured and modelled LDSA in different time windows at both stations. Two-sample t-tests were performed on the
328 two populations of absolute differences abovementioned to determine whether the difference between these ~~wais~~ statistically
329 significant. A significance level α of 5% ~~wais~~ chosen as the probability of rejecting the null hypothesis when it is true, denoted
330 as p .

331 4 LDSA measurement characterization

332 4.1 General characteristics of LDSA_{Pegasor} in Helsinki metropolitan area

333 The annual mean alveolar LDSA concentrations at four station types SC (2017–2018), UB (2017–May 2018), DH (2018) and
334 RB (2018) ~~are-were~~ $19.7 \pm 11.3 \mu\text{m}^2 \text{cm}^{-3}$, $11.2 \pm 7.1 \mu\text{m}^2 \text{cm}^{-3} \mu\text{g m}^{-3}$, $11.7 \pm 8.6 \mu\text{m}^2 \text{cm}^{-3}$ and $7.6 \pm 5.4 \mu\text{m}^2 \text{cm}^{-3}$, respectively
335 (Table 2). The DH and RB site ~~are-were~~ included to give more substantial interpretation of data because the LDSA
336 concentrations at RB can be viewed as background measurements and the local LDSA increments in HMA can be represented
337 by the LDSA at the hotspot measurement site subtracted by the LDSA at the RB site. The timeseries of LDSA concentrations
338 at the SC and the UB site ~~wereare~~ presented in Figure 3 and Fig. S4, where the missing data of LDSA for the whole
339 measurement period ~~wais~~ 3% and 30%, respectively. When comparing with the same site type in other cities around the globe,
340 LDSA concentrations detected in HMA ~~wereare~~ the lowest among the European cities with reported values, ~~and about one-~~
341 ~~fifth that in Japan (Table 1). While S~~ some literatures also reported LDSA at tracheobronchial region, ~~but~~ most just considered
342 LDSA at alveolar, which is considered to bring most harm to human's lungs, ~~as shown in Table 1~~ ~~Table 1~~.

343
344 The diurnal pattern of LDSA at RB ~~wais~~ not observable on workdays or over weekends (Figure 4, upper panel). The relatively
345 low variability can be explained by the scarcity of human activities. We can then regard the LDSA at RB as the background
346 concentrations mainly influenced by the regionally and long-range transported aerosol and meteorological variation (~~see~~
347 Luoma et al., 2021; Jafar and Harrison, 2021). As the concentrations at RB ~~wais~~ stable throughout the different hours of day;
348 therefore, the diurnal pattern of LDSA concentration ~~wais~~ apparently indistinguishable between the measured concentration
349 and the local increments. At the UB and DH site, the magnitudes and the patterns of the average hourly LDSA concentrations
350 at workdays ~~are-were~~ comparable, and both showed bimodal curves, one peak at 6–9 a.m., the other at 9–11 p.m.. The former
351 ~~hads~~ a larger peak during the morning peak hour because of the vehicular emissions (Timonen et al., 2013; Teinilä et al., 2019)
352 while the latter ~~hads~~ a larger peak in the evening attributed mainly by the residential burning (Hellén et al., 2017; Helin et al.,
353 2018; Luoma et al., 2021). Over weekends, the peaks in the morning ~~awerefe~~ not identifiable and the evening peaks ~~are-were~~
354 amplified due to enhanced human activities. Similar diurnal variation at residential- area was observed for BC emitted by

355 residential combustion by Helin et al. (2018). At the SC site, the morning peak on weekends was not obvious because of the
356 lack of work-related traffic. It appears that a similar bimodal curve can be seen during workdays, but the evening peak was
357 seen during the evening traffic rush hour around 4–6 p.m.. The reason was that the main contributor of LDSA at the SC site
358 was traffic and combustion processes and the diurnal variability mainly dependes on the citizen's movement by vehicles in
359 the city. Over weekends, the average hourly LDSA concentrations were the minimum at 5 a.m. and they increased and
360 remained at a high level at 2 p.m. until the late night. The level of LDSA concentrations at DH was comparable with that at
361 UB site. However, the amplitude of the evening peak was higher than that of the morning peak both on workdays and
362 weekends due to elevated residential combustion.

363

364 However, the monthly variability of background measurements at the RB site was stronger compared to the diurnal pattern
365 and the calculation of local increment was necessary (e.g. Jafar and Harrison, 2021). With no intense point sources, the
366 variations at RB were probably due to horizontal dispersion and advection of aerosol particles and vertical dilution controlled
367 by the boundary layer dynamics. Based on the monthly frequencies of backward trajectory by NOAA HYSPLIT Trajectory
368 Model (Rolph et al., 2017, Fig. S5), pollutants could be originated 600 km away from Helsinki within 24 hours in the winter.
369 In the summer, when solar radiation was persistently stronger, the boundary layer became elevated due to surface
370 heating and associated thermal turbulence. This turbulence would dilute the concentration of pollutants at the surface. Another
371 plausible reason could be the higher regional and long-range transported LDSA in the summer, as demonstrated by Kuula et
372 al. (2020) and Barreira et al. (2021). The lower panel in Figure 4 shows the LDSA local increments after subtraction of the
373 LDSA concentrations at the RB site. For instance, the local LDSA increments at DH are the highest in the winter probably due
374 to local small-scale wood combustion (and traffic). However, without subtracting the background concentrations, the LDSA
375 concentrations at DH were higher in the summer than in the winter (due to high regional background concentrations in
376 summer), as was observed also by Kuula et al. (2020). This piece of evidence can help in the source apportionment. The
377 variation of diurnal and seasonal LDSA for all sites are visualised in Fig. S65.

378 4.2 The connection between LDSA and other parameters

379 Alveolar LDSA concentration, as a single number, comprises particles across the whole particle size spectrum measured (e.g.
380 Pegasor AQ Urban ~10–400 nm). In HMA, the two local main sources of particles contributing to LDSA are vehicular
381 combustion and residential wood combustion emissions. Upon the two combustion processes, particles of different sizes and
382 different gaseous pollutants are emitted. A study by Lamberg et al. (2011) has shown that the geometric mean diameter of
383 residential wood combustion is typically 70–150 nm whereas Barreira et al. (2021) presented that the typical particle size for
384 vehicular combustion can be smaller than 50 nm. By calculating the proportion of LDSA with respect to different pollutant
385 parameters BC, NO_x, PNC (dominated by UFP), and PM_{2.5}, we could identify the contribution of LDSA across the hour of day
386 (Fig. S76 for workdays and Fig. S87 for weekends). Since the vehicular combustion emits smaller particles which elevate the
387 LDSA concentration but meanwhile do not substantially influence the value of PM_{2.5} (e.g. Salo et al., 2021a); therefore,
388 LDSA/PM_{2.5} hads a diurnal pattern similar to the LDSA concentrations which peaked in the morning rush hour during
389 workdays. Conversely, LDSA/BC, LDSA/PNC and LDSA/NO_x hadve a higher value before the morning rush hour and they
390 plunged in the morning rush hour. This can be explained by the fact that vehicular combustion caused high concentration
391 of BC, PNC and NO_x (Reche et al., 2015) compared to its contribution to LDSA concentration. In other words, the role of
392 regional background was higher for LDSA compared to those of NO_x, BC and PNC. At the UB site, the average LDSA/BC
393 at all hours remained at a constant level in the winter while the variability of the ratio was much higher in the summer. The
394 general LDSA/PNC ratio at UB was steadily 2–3 times higher than that at all hours in all seasons because the proportion of
395 larger particles at UB was usually higher than SC. This large variability again validated the heterogeneity of source of LDSA
396 at UB.

397

398 The integrated alveolar LDSA with a various size ranges was calculated to explore the correlation of size-fractionated LDSA
399 and other parameters in our multipollutant dataset. No single fractionated LDSA correlate~~s~~ well with meteorological
400 parameters at both sites (Figure 5). Out of all fractions, alveolar LDSA of the whole spectrum (LDSA_{6–800}) and LDSA_{250–400},
401 which explain~~s~~ majority of LDSA, correlate~~s~~ best with other air pollutants. In general, alveolar LDSA had~~s~~ a high
402 correlation with BC. BC correlate~~s~~ the best with LDSA_{100–250} ($r = 0.84$), which ~~was~~ in alignment with the reported values
403 from previous literatur~~s~~ (Gramsch et al., 2014; Ding et al., 2016). As expected, PM_{2.5} show~~e~~d better correlation with the
404 LDSA of larger particles ($r = 0.68–0.76$) because larger particles contributes more to PM_{2.5} mass concentration values. In the
405 meanwhile, PM₁₀ had~~s~~ fair correlation with all selected size bins. NO₂ correlate~~s~~ highly with LDSA of smaller particles ($r =$
406 $0.69–0.77$), indicating the dominant role of local traffic exhausts. CO had~~s~~ a higher correlation with LDSA of 400–800 nm ($r =$
407 0.64) since CO concentrations ~~were~~ more affected by regionally transported pollutants. O₃ had~~s~~ a fair correlation with
408 LDSA of all sections ($r = 0.30–0.43$) because the formation of O₃ is mostly secondary and the chemical interactions with
409 pollutants are more complicated than the other compounds. In general, the correlation~~s~~ of LDSA with other air pollutant
410 parameters ~~were~~ higher at the SC site than that at the UB site (Fig. S98). The high correlation~~s~~ of LDSA with BC, PM_{2.5} and
411 NO₂, which agree~~d~~ with the results by Kuula et al. (2020), prove~~d~~ the possibility of developing a model to estimate LDSA
412 concentrations.

413 5 Model evaluation

414 5.1 Sub-model diagnostics

415 Following the evaluation attributes described in Sect. 3.4,

417 **Table 3** depicts the descriptive statistics of the overall model evaluation on its testing set. The overall model at the SC site was
418 able to explain 80% of the variability of the testing set of the measured data. The R^2 in the winter was 0.86 being the highest
419 while the worst R^2 was shown in the summer, i.e., 0.70. The *MAE* and *cRMSD* ~~are~~ were the smallest during weekends with
420 R^2 not particularly high ($R^2 = 0.72$) probably because the LDSA concentration itself was relatively low in that period. The
421 overall performance was generally worse in UB in terms of R^2 , except during weekends that R^2 is 10% higher.

422
423 For individual sub-models, their performance could be seen on the Taylor's diagram in **Figure 6** (Taylor, 2001). Each
424 marker represents one sub-model, the contribution of which to the outcome of the final model is displayed in various colours.
425 The sub-model performance can be evaluated by the distance of the sub-model marker and the red point, which represents the
426 reference station, i.e., the perfect model. The location of each marker indicates its individual performance in terms of r (blue
427 contours), *cRMSD* (green contour) and *NSD* (black axis). At the SC site, the narrow distribution of the sub-models on the
428 Taylor's diagram gives a clue that they ~~are~~ were very similar in terms of model performance of LDSA estimation. The five
429 mostly used sub-models were concentrated within the region where r was 0.85–0.87, *cRMSD* was 5.67–5.77 $\mu\text{m}^2 \text{cm}^{-3}$ and
430 *NSD* was 0.75–0.79 (Table 4). The values of their evaluation metrics were close to each other where R^2 and *MAE* differed
431 in the narrow range of 10% ($R^2 = 0.72$ –0.74, *MAE* = 3.8 $\mu\text{m}^2 \text{cm}^{-3}$). It infers that if one metric was prioritised over another,
432 the rank of the sub-models can be greatly different. Although no individual sub-models showed r greater than 0.9, the overall
433 model comprising the outcomes by all the sub-models remained high ($R^2 = 0.80$, *MAE* = 3.8 $\mu\text{m}^2 \text{cm}^{-3}$). The best sub-model
434 was also the most used one, which accounted for 81% of the total data points while the two succeeding sub-models constituted
435 another 16%. This also indicates that the input adaptivity function of the suggested method supplemented 19% of the estimates,
436 which would be a missing estimate if a single model with fixed predictor variables was used. Four out of the five most used
437 sub-models contain BC as an input predictor with the combination of other two air pollutants or meteorological parameters.
438 This was in line with the high correlation of LDSA with BC ($r = 0.84$, Fig. S9) In case BC is missing at a certain time stamp,
439 the sub-model without BC as an input could be used. It further supports the input adaptive function.

440
441 At the UB site, the sub-model performance was more scattered on the Taylor's diagram (**Figure 6**). The five most
442 used sub-models had very varying metrics ($r = 0.77$ –0.92, *cRMSD* = 2.5–3.9 $\mu\text{m}^2 \text{cm}^{-3}$ and *NSD* = 0.63–0.89, see Table 5).
443 Although some showed exceptionally good performance, the overall model had a slightly worse performance than that in
444 street canyon. The best sub-model estimated 49% of the total measurement, followed by 17%. The third and fourth most used
445 sub-models, which formed up to 30% of the estimates, had rather moderate performance ($R^2 = 0.58$ and 0.69). Considering
446 all possible outcomes, the overall model was still able to explain 77% of the total variance. Despite the fair linear correlation
447 with LDSA, CO ($r = 0.26$) and PNC ($r = 0.71$) dominated in the top five used sub-models. This could be explained by the fact
448 that the source of CO can well cover the missing piece that PNC was unable to account for LDSA. BC, NO_x and meteorological
449 parameters, like RH and WD-N were also involved in the final LDSA estimation.

450
451 By checking the variance inflation factor (VIF) of all 696 sub-models, 4.6% and 2.2% were rejected respectively. The higher
452 rejection rate at SC can be explained by the fact that some of the predictor variables were highly correlating to each other and
453 the inclusion of them would result in an inflation of multi-collinearity of the sub-model, from which biases arise. At UB,
454 since the source of LDSA was more varied and the correlation of LDSA with other pollutants was generally lower, the
455 probability of the VIF of the individual sub-models exceeding the threshold was lower.

456 5.2 Temporal difference in comparison with other models

457 **Figure 7** presents the comparison of measured LDSA ($\text{LDSA}_{\text{Pegasor}}$), deposition model derived LDSA ($\text{LDSA}_{\text{ICRP}}$) and
458 the LDSA modelled by IAP and IAME (LDSA_{IAP} and $\text{LDSA}_{\text{IAME}}$) as a timeseries plot between 14 and 28 February 2017. This

459 particular time window ~~was~~ selected because it ~~suffers had~~ the least ~~in~~ data ~~missing gaps~~ for all the respective instruments at
460 both sites. This figure during this period can also showcase the difference in magnitudes of the diurnal shape over workdays
461 and weekends (shaded regions in ~~Figure 7~~Figure 7). At ~~the SC~~both sites, ~~both IAP and IAME underestimated the peaks when~~
462 ~~the change of the measured LDSA concentration was sudden and relatively large. However, this limitation did not diminish~~
463 ~~much of the usefulness of the models as virtual sensors as the models were still able to the estimates by both LDSA_{IAP} and~~
464 ~~LDSA_{IAME} could~~ generally catch up with the diurnal cycle of the measured data. ~~However, the models underestimate the peak~~
465 ~~if the change of the measured LDSA concentration is sudden and relatively large.~~ Despite the small difference observed in the
466 figure, the blue dotted line representing LDSA_{IAME} often stays closer to the measured LDSA concentration (black line). When
467 we smoothed out all the estimates at each hour, the ability for IAME to catch the morning peak on workdays ~~was~~ much better.
468 ~~At the UB site, IAME underestimates the LDSA concentration by almost 50% and 25% in the morning on 15 and 23 February~~
469 ~~2017, respectively. The overestimation reaches 100% during the midnight between 26 and 17 February 2017.~~

470
471 A more generalised diurnal cycle can be found in ~~Figure 8~~Figure 8. The error bars of the modelled LDSA_{IAP} and LDSA_{IAME}
472 ~~we~~are consistently smaller than that of LDSA_{Pegasor} and LDSA_{ICRP}. It might be due to the reason that the model fails to catch
473 the extreme values although it manageds to catch the general diurnal cycle. Since outliers ~~we~~are removed in the pre-processing
474 stage and the model penaliseds the extreme values, the model tendeds to give a more centralised estimate. It ~~was~~ a trade-off
475 between the option with better coefficients of determination but stronger extreme errors and that with better estimations at tails
476 but derivation of averaged estimation. This circumstance ~~was~~ more apparent on workdays than weekends. Furthermore,
477 LDSA_{IAME} could follow the diurnal cycle of LDSA_{Pegasor} much better than LDSA_{IAP}, especially during the start of the peak
478 hours over workdays at the SC site where the LDSA concentrations jumped to a high level. LDSA_{IAME} can explain 80% and
479 77% of the variability of the reference measurements at SC and UB, respectively (Table 6), and compared to LDSA_{IAP}'s 77%
480 and 66%, LDSA_{IAME} performed better in terms of accuracy. In addition, the slightly smaller MAE and the closer to 1 NSD of
481 the LDSA_{IAME} suggested that the mean absolute error ~~was~~ improved and the spread of the estimation distribution ~~was~~ closer
482 to the reference measurement by taking random effects into account.

483
484 Furthermore, we assessed the temporal and spatial impact on the IAME model by comparing the means of absolute differences
485 between the hourly LDSA_{Pegasor} and LDSA_{IAME} in different time windows at both stations. A descriptive statistic is presented
486 in Table 7. We used two-sample t-tests to assess whether the distribution of absolute differences were statistically significant.
487 At SC, the *p* value of the t-tests at all selected windows ~~we~~are below 0.05, which demonstrated that the performance at different
488 seasons, days of week and hours of day of absolute differences between the measured and modelled LDSA were significantly
489 different at the confidential level of 95%. At the UB site, the difference between the two selected hour periods ~~was~~ not
490 statistically significant. The same applieds to the difference between winter and spring. There ~~was~~are no statistically sufficient
491 evidence to validate the difference among the rest of the selected time period. In other words, with the use of random effects
492 of time constraint, the overall models still performed differently at different time windows most of the time. This indicates that
493 IAME still needs improvements on minimising temporal differences.

494 6 Conclusion

495 In this study, we developed a novel input-adaptive mixed-effects (IAME) proxy, to estimate alveolar LDSA by other already
496 existing air pollutant variables and meteorological conditions in Helsinki Metropolitan Area. During the measurement period
497 2017–2018, we retrieved LDSA measurements measured by Pegasor AQ Urban (alveolar LDSA in the ~10–400 size range)
498 and other variables in a street canyon (SC, average LDSA = 19.7±11.3 μm² cm⁻³) site and an urban background (UB, average
499 LDSA = 11.2±7.1 μm² cm⁻³) site in Helsinki, Finland. Furthermore, three detached housing sites (DH, average LDSA =

500 $11.7 \pm 8.6 \mu\text{m}^2 \text{cm}^{-3}$) and a regional background site (RB, average LDSA = $7.6 \pm 5.4 \mu\text{m}^2 \text{cm}^{-3}$) ~~we~~are also included as reference
501 and background source estimation, respectively. At the SC site, LDSA concentrations ~~we~~are closely correlated with traffic
502 emission. The ratio to black carbon (LDSA/BC), to particle number concentration (LDSA/PNC), and to nitrogen oxide
503 (LDSA/ NO_x) had ~~ve~~ a higher value before the morning peak and it reached ~~s~~ its minimum during the morning peak since the
504 role of regional background ~~wa~~is higher for LDSA compared to those of NO_x , BC and PNC. However, the ratio of LDSA to
505 mass concentration of particles of diameter smaller than $2.5 \mu\text{m}$ (LDSA/ $\text{PM}_{2.5}$) performed ~~ed~~ differently since the freshly
506 vehicular emitted particles ~~we~~are smaller than 50 nm , which ~~di~~do not contribute much to $\text{PM}_{2.5}$ mass concentration.

507
508 For the continuous estimation of LDSA, IAME ~~wa~~is automatised to select the best combination of input variables, including
509 a maximum of three fixed effect variables and three time indicators as random effect variables. Altogether, 696 sub-models
510 ~~we~~are generated and ranked by the coefficient of determination (R^2), mean absolute error (MAE) and centred root-mean-
511 square differences ($cRMSD$) in order. At the SC site, LDSA concentrations can be best estimated by $\text{PM}_{2.5}$, PNC and BC, all
512 of which ~~we~~are closely connected with the vehicular emissions, while they ~~we~~are found correlating with $\text{PM}_{2.5}$, BC and carbon
513 monoxide (CO) the best at the UB site. At both sites, $\text{PM}_{2.5}$ also indicated ~~s~~ the regionally and long-range transported pollutants,
514 which ~~wa~~is a significant source of LDSA concentrations. The accuracy of the overall model ~~wa~~is higher at the SC site ($R^2 =$
515 0.80 , $MAE = 3.7 \mu\text{m}^2 \text{cm}^{-3}$) than at the UB site ($R^2 = 0.77$, $MAE = 2.3 \mu\text{m}^2 \text{cm}^{-3}$) plausibly because the LDSA source was
516 more tightly controlled by the close-by vehicular emission source. This model could catch the temporal pattern of LDSA;
517 however, the two-sample t-tests of the residuals at all selected time windows showed ~~ed~~ that their distributions ~~we~~are different.
518 This indicated ~~s~~ that the model still performed ~~s~~ differently at different time windows. Despite this, the novel IMAE model
519 worked ~~s~~ better in explaining the variability of the measurements than the previously suggested IAP model as indicated by a
520 higher R^2 and lower MAE in both sites. This adjustment by taking random effects into account improved ~~s~~ the sensitivity and
521 the accuracy of the fixed effect model IAP.

522
523 The models alone cannot replace the need for reference measurements (Hagler et al., 2018). However, the IAME proxy could
524 serve as virtual sensors to complement the measurements at reference stations in case of missing data. The two measurement
525 sites in this study served ~~d~~ as a pilot of the proxy development, and the next step is to extend the work to the existing network
526 of several measurement stations within the Helsinki metropolitan region. With similar configurations, we could fill up the
527 voids with the information from the other stations after conscientious calibration. For example, in this paper, the two
528 measurement sites ~~we~~are characterised as street canyon and urban background. In a different setup, we may assume the
529 similarity of the same type of environment and utilise the measurements as replacement.

530
531 Furthermore, this continuous LDSA estimation could be useful in updating some of the current air quality application, for
532 instance ~~GreenPaths application which searches for the best route to wished destination with the least exposure to air pollution~~
533 ~~(Poem et al., 2020) and~~ ENFUSER air quality model which provide accurate spatio-temporal estimation for air pollutants in
534 Helsinki (Johansson et al., 2015).

535

536 **Data availability**

537 The air quality data and meteorological data are available from HSY website (<https://www.hsy.fi/avoindata>) and through
538 SmartSMEAR online tool (<https://smear.avaa.csc.fi/>).

539 **Author contributions**

540 PLF performed formal analysis and writing – original draft of the manuscript. PLF, MAZ, TP and TH conceptualized and
541 designed the methodology of this work. MAZ, ST, MK, TP and TH provided supervision in this research activity. ES (Pegasor
542 Ltd.), JVN and AKo (HSY), and HT, JK and AKa (FMI) provided instruments and data for the campaign. All the co-authors
543 (MAZ, JVN, ES, HT, AKo, JK, TR, Aka, ST, MK, TP and TH) reviewed and commented on the manuscript.

544 **Competing interests**

545 Prof. Markku Kulmala and Prof. Tuukka Petäjä are members of the editorial board of the journal Atmospheric Chemistry and
546 Physics. Dr. Erkkä Saukko works in Pegasor Ltd. which is the manufacturer of Pegasor AQ Urban.

547 **Acknowledgements**

548 The authors acknowledge the City of Helsinki for providing traffic count data.

549 **Financial support**

550 This work is supported by the European Regional Development Fund through the Urban Innovative Action (project HOPE;
551 Healthy Outdoor Premises for Everyone, project no. UIA03-240) and Regional Innovations and Experimentations Fund AIKO,
552 governed by the Helsinki Regional Council (project HAQT; Helsinki Air Quality Testbed, project no. AIKO014). Grants are
553 also received from the European Research Council through the European Union's Horizon 2020 Research and Innovation
554 Framework Program (grant agreement no. 742206), and ERA-PLANET (www.era-planet.eu) and its trans-national project
555 SMURBS (www.smurbs.eu) funded under the same program (grant agreement no. 689443). The authors show gratitude to
556 Academy of Finland for the funding via the Academy of Finland Flagship funding (project no. 337549 and 337552) and
557 NanoBioMass (project no. 1307537).

558 **References**

- 559 Albuquerque, P. C., Gomes, J. F., and Bordado, J. C.: Assessment of exposure to airborne ultrafine particles in the urban
560 environment of Lisbon, Portugal, *J. Air Waste Manag. Assoc.*, 62, 373-380, <https://doi.org/10.1080/10962247.2012.658957>,
561 2012.
- 562 Amanatidis, S., Maricq, M. M., Ntziachristos, L., and Samaras, Z.: Application of the dual Pegasor Particle Sensor to real-
563 time measurement of motor vehicle exhaust PM, *J. Aerosol Sci.*, 103, 93-104, <https://doi.org/10.1016/j.jaerosci.2016.10.005>,
564 2017.
- 565 Anjilvel, S., and Asgharian, B.: A multiple-path model of particle deposition in the rat lung, *Fund. Appl. Toxicol.*, 28, 41-50,
566 <https://doi.org/10.1006/faat.1995.1144>, 1995.
- 567 Asbach, C., Fissan, H., Stahlmecke, B., Kuhlbusch, T., and Pui, D.: Conceptual limitations and extensions of lung-deposited
568 Nanoparticle Surface Area Monitor (NSAM), *J. Nanopart. Res.*, 11, 101-109, <https://doi.org/10.1007/s11051-008-9479-8>,
569 2009.
- 570 Asbach, C., Alexander, C., Clavaguera, S., Dahmann, D., Dozol, H., Faure, B., Fierz, M., Fontana, L., Iavicoli, I., Kaminski,
571 H., MacCalman, L., Meyer-Plath, A., Simonow, B., van Tongeren, M., and Todea, A. M.: Review of measurement techniques
572 and methods for assessing personal exposure to airborne nanomaterials in workplaces, *Sci. Total Environ.*, 603, 793-806,
573 <https://doi.org/10.1016/j.scitotenv.2017.03.049>, 2017.
- 574 Barreira, L. M. F., Helin, A., Aurela, M., Teinilä, K., Friman, M., Kangas, L., Niemi, J. V., Portin, H., Kousa, A., Pirjola, L.,
575 Rönkkö, T., Saarikoski, S., and Timonen, H.: In-depth characterization of submicron particulate matter inter-annual variations
576 at a street canyon site in northern Europe, *Atmos. Chem. Phys.*, 21, 6297-6314, <https://doi.org/10.5194/acp-21-6297-2021>,
577 2021.
- 578 Breiman, L.: Heuristics of instability and stabilization in model selection, *Ann. Stat.*, 24, 2350-2383,
579 <https://doi.org/10.1214/aos/1032181158>, 1996.

580 Brown, D. M., Wilson, M. R., MacNee, W., Stone, V., and Donaldson, K.: Size-dependent proinflammatory effects of ultrafine
581 polystyrene particles: a role for surface area and oxidative stress in the enhanced activity of ultrafines, *Toxicol. Appl. Pharm.*,
582 175, 191-199, <https://doi.org/10.1006/taap.2001.9240>, 2001.

583 Buonanno, G., Marini, S., Morawska, L., and Fuoco, F. C.: Individual dose and exposure of Italian children to ultrafine
584 particles, *Sci. Total Environ.*, 438, 271-277, <https://doi.org/10.1016/j.scitotenv.2012.08.074>, 2012.

585 Cabaneros, S. M., Calautit, J. K., and Hughes, B. R.: A review of artificial neural network models for ambient air pollution
586 prediction, *Environ. Modell. Softw.*, 119, 285-304, <https://doi.org/10.1016/j.envsoft.2019.06.014>, 2019.

587 Chen, J., de Hoogh, K., Gulliver, J., Hoffmann, B., Hertel, O., Ketzler, M., Bauwelinck, M., van Donkelaar, A., Hvidtfeldt, U.
588 A., Katsouyanni, K., Janssen, N. A. H., Martin, R. V., Samoli, E., Schwartz, P. E., Stafoggia, M., Bellander, T., Strak, M.,
589 Wolf, K., Vienneau, D., Vermeulen, R., Brunekreef, B., and Hoek, G.: A comparison of linear regression, regularization, and
590 machine learning algorithms to develop Europe-wide spatial models of fine particles and nitrogen dioxide, *Environ. Int.*, 130,
591 104934, <https://doi.org/10.1016/j.envint.2019.104934>, 2019.

592 Cheristanidis, S., Grivas, G., and Chaloulakou, A.: Determination of total and lung-deposited particle surface area
593 concentrations, in central Athens, Greece, *Environ. Monit. Assess.*, 192, 627, <https://doi.org/10.1007/s10661-020-08569-8>,
594 2020.

595 Chudnovsky, A. A., Lee, H. J., Kostinski, A., Kotlov, T., and Koutrakis, P.: Prediction of daily fine particulate matter
596 concentrations using aerosol optical depth retrievals from the Geostationary Operational Environmental Satellite (GOES), *J.*
597 *Air Waste Manag. Assoc.*, 62, 1022-1031, <https://doi.org/10.1080/10962247.2012.695321>, 2012.

598 Dal Maso, M., Gao, J., Järvinen, A., Li, H., Luo, D., Janka, K., and Rönkkö, T.: Improving urban air quality measurements by
599 a diffusion charger based electrical particle sensors-A field study in Beijing, China, *Aerosol Air Qual. Res.*, 16, 3001-3011,
600 <https://doi.org/10.4209/aaqr.2015.09.0546>, 2016.

601 Ding, A., Huang, X., Nie, W., Sun, J., Kerminen, V. M., Petäjä, T., Su, H., Cheng, Y., Yang, X. Q., and Wang, M.: Enhanced
602 haze pollution by black carbon in megacities in China, *Geophys. Res. Lett.*, 43, 2873-2879,
603 <https://doi.org/10.1002/2016GL067745>, 2016.

604 Dockery, D. W., Pope, C. A., Xu, X., Spengler, J. D., Ware, J. H., Fay, M. E., Ferris Jr, B. G., and Speizer, F. E.: An association
605 between air pollution and mortality in six US cities, *New Engl. J. Med.*, 329, 1753-1759,
606 <https://doi.org/10.1056/NEJM199312093292401>, 1993.

607 Duffin, R., Tran, C., Clouter, A., Brown, D., MacNee, W., Stone, V., and Donaldson, K.: The importance of surface area and
608 specific reactivity in the acute pulmonary inflammatory response to particles, *Ann. Occup. Hyg.*, 46, 242-245,
609 <https://doi.org/10.1093/annhyg/mef684>, 2002.

610 Eeftens, M., Meier, R., Schindler, C., Aguilera, I., Phuleria, H., Ineichen, A., Davey, M., Ducret-Stich, R., Keidel, D., Probst-
611 Hensch, N., Kunzli, N., and Tsai, M. Y.: Development of land use regression models for nitrogen dioxide, ultrafine particles,
612 lung deposited surface area, and four other markers of particulate matter pollution in the Swiss SAPALDIA regions, *Environ.*
613 *Health*, 15, 53, <https://doi.org/10.1186/s12940-016-0137-9>, 2016.

614 Faraway, J. J.: *Linear models with R*, CRC press, 2014.

615 Fernández-Guisuraga, J. M., Castro, A., Alves, C., Calvo, A., Alonso-Blanco, E., Blanco-Alegre, C., Rocha, A., and Fraile,
616 R.: Nitrogen oxides and ozone in Portugal: trends and ozone estimation in an urban and a rural site, *Environ. Sci. Pollut. R.*,
617 23, 17171-17182, <https://doi.org/10.1007/s11356-016-6888-6>, 2016.

618 Fissan, H., Neumann, S., Trampe, A., Pui, D., and Shin, W.: Rationale and principle of an instrument measuring lung deposited
619 nanoparticle surface area, *J. Nanopart. Res.*, 53-59, <https://doi.org/10.1007/s11051-006-9156-8>, 2006.

620 Fung, P. L., Zaidan, M. A., Sillanpaa, S., Kousa, A., Niemi, J. V., Timonen, H., Kuula, J., Saukko, E., Luoma, K., Petaja, T.,
621 Tarkoma, S., Kulmala, M., and Hussein, T.: Input-Adaptive Proxy for Black Carbon as a Virtual Sensor, *Sensors (Basel)*, 20,
622 <https://doi.org/10.3390/s20010182>, 2020.

623 Fung, P. L., Zaidan, M. A., Surakhi, O., Tarkoma, S., Petäjä, T., and Hussein, T.: Data imputation in in situ-measured particle
624 size distributions by means of neural networks, *Atmos. Meas. Tech.*, 14, 5535-5554, [https://doi.org/10.5194/amt-14-5535-](https://doi.org/10.5194/amt-14-5535-2021)
625 [2021](https://doi.org/10.5194/amt-14-5535-2021), 2021a.

626 Fung, P. L., Zaidan, M. A., Timonen, H., Niemi, J. V., Kousa, A., Kuula, J., Luoma, K., Tarkoma, S., Petäjä, T., Kulmala, M.,
627 and Hussein, T.: Evaluation of white-box versus black-box machine learning models in estimating ambient black carbon
628 concentration, *J. Aerosol Sci.*, <https://doi.org/10.1016/j.jaerosci.2020.105694>, 2021b.

629 Gramsch, E., Reyes, F., Oyola, P., Rubio, M., López, G., Pérez, P., and Martínez, R.: Particle size distribution and its
630 relationship to black carbon in two urban and one rural site in Santiago de Chile, *J. Air Waste Manag. Assoc.*, 64, 785-796,
631 <https://doi.org/10.1080/10962247.2014.890141>, 2014.

632 Gupta, R., and Xie, H.: Nanoparticles in daily life: applications, toxicity and regulations, *J. Environ. Pathol. Tox.*, 37,
633 <https://doi.org/10.1615/JEnvironPatholToxicolOncol.2018026009>, 2018.

634 Habre, R., Zhou, H., Eckel, S. P., Enebish, T., Fruin, S., Bastain, T., Rappaport, E., and Gilliland, F.: Short-term effects of
635 airport-associated ultrafine particle exposure on lung function and inflammation in adults with asthma, *Environ. Int.*, 118, 48-
636 59, <https://doi.org/10.1016/j.envint.2018.05.031>, 2018.

637 Hagler, G. S. W., Williams, R., Papapostolou, V., and Polidori, A.: Air Quality Sensors and Data Adjustment Algorithms:
638 When Is It No Longer a Measurement?, *Environ. Sci. Technol.*, 52, 5530-5531,
639 <https://pubs.acs.org/doi/10.1021/acs.est.8b01826>, 2018.

640 Hama, S. M. L., Ma, N., Cordell, R. L., Kos, G. P. A., Wiedensohler, A., and Monks, P. S.: Lung deposited surface area in
641 Leicester urban background site/UK: Sources and contribution of new particle formation, *Atmos. Environ.*, 151, 94-107,
642 <https://doi.org/10.1016/j.atmosenv.2016.12.002>, 2017.

643 Hastie, T., Tibshirani, R., and Tibshirani, R.: Best Subset, Forward Stepwise or Lasso? Analysis and Recommendations Based
644 on Extensive Comparisons, *Stat. Sci.*, 35, 579-592, <https://doi.org/10.1214/19-STS733>, 2020.

645 Helin, A., Niemi, J. V., Virkkula, A., Pirjola, L., Teinilä, K., Backman, J., Aurela, M., Saarikoski, S., Rönkkö, T., Asmi, E.,
646 and Timonen, H.: Characteristics and source apportionment of black carbon in the Helsinki metropolitan area, Finland, *Atmos.*
647 *Environ.*, 190, 87-98, <https://doi.org/10.1016/j.atmosenv.2018.07.022>, 2018.

648 Hellén, H., Kangas, L., Kousa, A., Vestenius, M., Teinilä, K., Karppinen, A., Kukkonen, J., and Niemi, J. V.: Evaluation of
649 the impact of wood combustion on benzo [a] pyrene (BaP) concentrations; ambient measurements and dispersion modeling in
650 Helsinki, Finland, *Atmos. Chem. Phys.*, 17, 3475-3487, <https://doi.org/10.5194/acp-17-3475-2017>, 2017.

651 Hennig, F., Quass, U., Hellack, B., Kupper, M., Kuhlbusch, T. A. J., Stafoggia, M., and Hoffmann, B.: Ultrafine and Fine
652 Particle Number and Surface Area Concentrations and Daily Cause-Specific Mortality in the Ruhr Area, Germany, 2009-2014,
653 *Environ. Health Persp.*, 126, 027008, <https://doi.org/10.1289/EHP2054>, 2018.

654 Hinds, W. C.: Aerosol technology: properties, behavior, and measurement of airborne particles, John Wiley & Sons, 1999.

655 Hofmann, W.: Modelling particle deposition in human lungs: modelling concepts and comparison with experimental data,
656 *Biomarkers*, 14, 59-62, <https://doi.org/10.1080/13547500902965120>, 2009.

657 ICRP: PUBLICATION 66: Human Respiratory Tract Model for Radiological Protection, Pergamon Press, New York, 1994.

658 Jafar, H. A., and Harrison, R. M.: Spatial and temporal trends in carbonaceous aerosols in the United Kingdom, *Atmos. Pollut.*
659 *Res.*, 12, 295-305, <https://doi.org/10.1016/j.apr.2020.09.009>, 2021.

660 Järvi, L., Hannuniemi, H., Hussein, T., Junninen, H., Aalto, P. P., Hillamo, R., Mäkelä, T., Keronen, P., Siivola, E., and Vesala,
661 T.: The urban measurement station SMEAR III: Continuous monitoring of air pollution and surface-atmosphere interactions
662 in Helsinki, Finland, *Boreal Environ. Res.*, 19, 86-109, 2009.

663 Järvinen, A., Kuuluvainen, H., Niemi, J. V., Saari, S., Dal Maso, M., Pirjola, L., Hillamo, R., Janka, K., Keskinen, J., and
664 Rönkkö, T.: Monitoring urban air quality with a diffusion charger based electrical particle sensor, *Urban Clim.*, 14, 441-456,
665 <https://doi.org/10.1016/j.uclim.2014.10.002>, 2015.

666 Järvinen, A., Timonen, H., Karjalainen, P., Bloss, M., Simonen, P., Saarikoski, S., Kuuluvainen, H., Kalliokoski, J., Dal Maso,
667 M., Niemi, J. V., Keskinen, J., and Rönkkö, T.: Particle emissions of Euro VI, EEV and retrofitted EEV city buses in real
668 traffic, *Environ. Pollut.*, 250, 708-716, <https://doi.org/10.1016/j.envpol.2019.04.033>, 2019.

669 Johansson, L., Epitropou, V., Karatzas, K., Karppinen, A., Wanner, L., Vrochidis, S., Bassoukos, A., Kukkonen, J., and
670 Kompatsiaris, I.: Fusion of meteorological and air quality data extracted from the web for personalized environmental
671 information services, *Environ. Modell. Softw.*, 64, 143-155, <https://doi.org/10.1016/j.envsoft.2014.11.021>, 2015.

672 Karjalainen, P., Timonen, H., Saukko, E., Kuuluvainen, H., Saarikoski, S., Aakko-Saksa, P., Murtonen, T., Bloss, M., Maso,
673 M. D., Simonen, P., Ahlberg, E., Svenningsson, B., Brune, W. H., Hillamo, R., Keskinen, J., and Rönkkö, T.: Time-resolved
674 characterization of primary particle emissions and secondary particle formation from a modern gasoline passenger car, *Atmos.*
675 *Chem. Phys.*, 16, 8559-8570, <https://doi.org/10.5194/acp-16-8559-2016>, 2016.

676 Kiriya, M., Okuda, T., Yamazaki, H., Hatoya, K., Kaneyasu, N., Uno, I., Nishita, C., Hara, K., Hayashi, M., Funato, K., Inoue,
677 K., Yamamoto, S., Yoshino, A., and Takami, A.: Monthly and Diurnal Variation of the Concentrations of Aerosol Surface
678 Area in Fukuoka, Japan, Measured by Diffusion Charging Method, *Atmosphere (Basel)*, 8,
679 <https://doi.org/10.3390/atmos8070114>, 2017.

680 Kulkarni, P., Baron, P. A., and Willeke, K.: Aerosol measurement: principles, techniques, and applications, John Wiley &
681 Sons, 2011.

682 Kuula, J., Kuuluvainen, H., Rönkkö, T., Niemi, J. V., Saukko, E., Portin, H., Aurela, M., Saarikoski, S., Rostedt, A., Hillamo,
683 R., and Timonen, H.: Applicability of Optical and Diffusion Charging-Based Particulate Matter Sensors to Urban Air Quality
684 Measurements, *Aerosol Air Qual. Res.*, 19, 1024-1039, <https://doi.org/10.4209/aaqr.2018.04.0143>, 2019.

685 Kuula, J., Kuuluvainen, H., Niemi, J. V., Saukko, E., Portin, H., Kousa, A., Aurela, M., Rönkkö, T., and Timonen, H.: Long-
686 term sensor measurements of lung deposited surface area of particulate matter emitted from local vehicular and residential
687 wood combustion sources, *Aerosol Sci. Tech.*, 54, 190-202, <https://doi.org/10.1080/02786826.2019.1668909>, 2020.

688 Kuuluvainen, H., Rönkkö, T., Järvinen, A., Saari, S., Karjalainen, P., Lähde, T., Pirjola, L., Niemi, J. V., Hillamo, R., and
689 Keskinen, J.: Lung deposited surface area size distributions of particulate matter in different urban areas, *Atmos. Environ.*,
690 136, 105-113, <https://doi.org/10.1016/j.atmosenv.2016.04.019>, 2016.

691 Kuuluvainen, H., Poikkimäki, M., Järvinen, A., Kuula, J., Irjala, M., Dal Maso, M., Keskinen, J., Timonen, H., Niemi, J. V.,
692 and Ronkko, T.: Vertical profiles of lung deposited surface area concentration of particulate matter measured with a drone in
693 a street canyon, *Environ. Pollut.*, 241, 96-105, <https://doi.org/10.1016/j.envpol.2018.04.100>, 2018.

694 Lamberg, H., Nuutinen, K., Tissari, J., Ruusunen, J., Yli-Pirilä, P., Sippula, O., Tapanainen, M., Jalava, P., Makkonen, U.,
695 Teinilä, K., Saarnio, K., Hillamo, R., Hirvonen, M.-R., and Jokiniemi, J.: Physicochemical characterization of fine particles
696 from small-scale wood combustion, *Atmos. Environ.*, 45, 7635-7643, <https://doi.org/10.1016/j.atmosenv.2011.02.072>, 2011.

697 Lindstrom, M. J., and Bates, D. M.: Newton—Raphson and EM algorithms for linear mixed-effects models for repeated-
698 measures data, *J. Am. Stat. Assoc.*, 83, 1014-1022, <https://doi.org/10.2307/2290128>, 1988.

699 Liu, H., Zhang, X., Zhang, H., Yao, X., Zhou, M., Wang, J., He, Z., Zhang, H., Lou, L., Mao, W., Zheng, P., and Hu, B.: Effect
700 of air pollution on the total bacteria and pathogenic bacteria in different sizes of particulate matter, *Environ. Pollut.*, 233, 483-
701 493, <https://doi.org/10.1016/j.envpol.2017.10.070>, 2018a.

702 Liu, Y., Wu, J., Yu, D., and Hao, R.: Understanding the patterns and drivers of air pollution on multiple time scales: the case
703 of northern China, *Environ. Manage.*, 61, 1048-1061, <https://doi.org/10.1007/s00267-018-1026-5>, 2018b.

704 Luoma, K., Niemi, J. V., Aurela, M., Fung, P. L., Helin, A., Hussein, T., Kangas, L., Kousa, A., Rönkkö, T., Timonen, H.,
705 Virkkula, A., and Petäjä, T.: Spatiotemporal variation and trends in equivalent black carbon in the Helsinki metropolitan area
706 in Finland, *Atmos. Chem. Phys.*, 21, 1173-1189, <https://doi.org/10.5194/acp-21-1173-2021>, 2021.

707 Maricq, M. M.: Monitoring Motor Vehicle PM Emissions: An Evaluation of Three Portable Low-Cost Aerosol Instruments,
708 *Aerosol Sci. Tech.*, 47, 564-573, <https://doi.org/10.1080/02786826.2013.773394>, 2013.

709 Mikkonen, S., Németh, Z., Varga, V., Weidinger, T., Leinonen, V., Yli-Juuti, T., and Salma, I.: Decennial time trends and
710 diurnal patterns of particle number concentrations in a central European city between 2008 and 2018, *Atmos. Chem. Phys.*,
711 20, 12247-12263, <https://doi.org/10.5194/acp-20-12247-2020>, 2020.

712 Miller, A.: *Subset selection in regression*, CRC Press, 2002.

713 NCRP: Report No. 125: Deposition, Retention and Dosimetry of Inhaled Radioactive Substances, National Council on
714 Radiation Protection and Measurements, 1997.

715 Oberdorster, G.: Nanotoxicology: in vitro-in vivo dosimetry, *Environ. Health Persp.*, 120, A13; author reply A13,
716 <https://doi.org/10.1289/ehp.1104320>, 2012.

717 Oberdorster, G., Maynard, A., Donaldson, K., Castranova, V., Fitzpatrick, J., Ausman, K., Carter, J., Karn, B., Kreyling, W.,
718 Lai, D., Olin, S., Monteiro-Riviere, N., Warheit, D., Yang, H., and A report from the ILSI Research Foundation/Risk Science
719 Institute Nanomaterial Toxicity Screening Working Group: Principles for characterizing the potential human health effects
720 from exposure to nanomaterials: elements of a screening strategy, Part. *Fibre Toxicol.*, 2, 1-35, <https://doi.org/10.1186/1743-8977-2-8>, 2005.

722 Pacitto, A., Stabile, L., Russo, S., and Buonanno, G.: Exposure to Submicron Particles and Estimation of the Dose Received
723 by Children in School and Non-School Environments, *Atmosphere (Basel)*, 11, <https://doi.org/10.3390/atmos11050485>, 2020.

724 Petäjä, T., Kerminen, V.-M., Maso, M. D., Junninen, H., Koponen, I., Hussein, T., Aalto, P. P., Andronopoulos, S., Robin, D.,
725 Hämeri, K., Bartzis, J. G., and Kulmala, M.: Sub-micron atmospheric aerosols in the surroundings of Marseille and Athens:
726 physical characterization and new particle formation, *Atmos. Chem. Phys.*, 7, 2705-2720, <https://doi.org/10.5194/acp-7-2705-2007>, 2007.

728 Pirjola, L., Niemi, J. V., Saarikoski, S., Aurela, M., Enroth, J., Carbone, S., Saarnio, K., Kuuluvainen, H., Kousa, A., Rönkkö,
729 T., and Hillamo, R.: Physical and chemical characterization of urban winter-time aerosols by mobile measurements in Helsinki,
730 *Finland, Atmos. Environ.*, 158, 60-75, <https://doi.org/10.1016/j.atmosenv.2017.03.028>, 2017.

731 Reche, C., Viana, M., Brines, M., Perez, N., Beddows, D., Alastuey, A., and Querol, X.: Determinants of aerosol lung-
732 deposited surface area variation in an urban environment, *Sci. Total Environ.*, 517, 38-47,
733 <https://doi.org/10.1016/j.scitotenv.2015.02.049>, 2015.

734 Rolph, G., Stein, A., and Stunder, B.: Real-time Environmental Applications and Display sYstem: READY, *Environ. Model.*
735 *Softw.*, 95, 210-228, <https://doi.org/10.1016/j.envsoft.2017.06.025>, 2017.

736 Rönkkö, T., Kuuluvainen, H., Karjalainen, P., Keskinen, J., Hillamo, R., Niemi, J. V., Pirjola, L., Timonen, H. J., Saarikoski,
737 S., Saukko, E., Järvinen, A., Silvennoinen, H., Rostedt, A., Olin, M., Yli-Ojanperä, J., Nousiainen, P., Kousa, A., and Dal
738 Maso, M.: Traffic is a major source of atmospheric nanocluster aerosol, *Proc. Natl. Acad. Sci. U.S.A.*, 114, 7549-7554,
739 <https://doi.org/10.1073/pnas.1700830114>, 2017.

740 Rostedt, A., Arffman, A., Janka, K., Yli-Ojanperä, J., and Keskinen, J.: Characterization and Response Model of the PPS-M
741 Aerosol Sensor, *Aerosol Sci. Tech.*, 48, 1022-1030, <https://doi.org/10.1080/02786826.2014.951023>, 2014.

742 Rudin, C.: Stop explaining black box machine learning models for high stakes decisions and use interpretable models instead,
743 *Nat. Mach. Intell.*, 1, 206-215, <https://doi.org/10.1038/s42256-019-0048-x>, 2019.

744 Salo, L., Hyvärinen, A., Jalava, P., Teinilä, K., Hooda, R. K., Datta, A., Saarikoski, S., Lintusaari, H., Lepistö, T., Martikainen,
745 S., Rostedt, A., Sharma, V. P., Rahman, M. H., Subudhi, S., Asmi, E., Niemi, J. V., Lihavainen, H., Lal, B., Keskinen, J.,
746 Kuuluvainen, H., Timonen, H., and Rönkkö, T.: The characteristics and size of lung-depositing particles vary significantly
747 between high and low pollution traffic environments, *Atmos. Environ.*, 118421,
748 <https://doi.org/10.1016/j.atmosenv.2021.118421>, 2021a.

749 Salo, L., Rönkkö, T., Saarikoski, S., Teinilä, K., Kuula, J., Alanen, J., Arffman, A., Timonen, H., and Keskinen, J.:
750 Concentrations and Size Distributions of Particle Lung-deposited Surface Area (LDSA) in an Underground Mine, *Aerosol Air*
751 *Qual. Res.*, 21, 200660-200660, <https://doi.org/10.4209/aaqr.200660>, 2021b.

752 Schmid, O., and Stoeger, T.: Surface area is the biologically most effective dose metric for acute nanoparticle toxicity in the
753 lung, *J. Aerosol Sci.*, 99, 133-143, <https://doi.org/10.1016/j.jaerosci.2015.12.006>, 2016.

754 Shiraiwa, M., Ueda, K., Pozzer, A., Lammel, G., Kampf, C. J., Fushimi, A., Enami, S., Arangio, A. M., Fröhlich-Nowoisky,
755 J., Fujitani, Y., Furuyama, A., Lakey, P. S. J., Lelieveld, J., Lucas, K., Morino, Y., Pöschl, U., Takahama, S., Takami, A.,
756 Tong, H., Weber, B., Yoshino, A., and Sato, K.: Aerosol health effects from molecular to global scales, *Environ. Sci. Technol.*,
757 51, 13545-13567, <https://doi.org/10.1021/acs.est.7b04417>, 2017.

758 Šimić, I., Lovrić, M., Godec, R., Kröll, M., and Bešlić, I.: Applying machine learning methods to better understand, model
759 and estimate mass concentrations of traffic-related pollutants at a typical street canyon, *Environ. Pollut.*, 263, 114587,
760 <https://doi.org/10.1016/j.envpol.2020.114587>, 2020.

761 Taylor, K. E.: Summarizing multiple aspects of model performance in a single diagram, *J. Geophys. Res. Atmos.*, 106, 7183-
762 7192, <https://doi.org/10.1029/2000JD900719>, 2001.

763 Teinilä, K., Aurela, M., Niemi, J. V., Kousa, A., Petäjä, T., Järvi, L., Hillamo, R., Kangas, L., Saarikoski, S., and Timonen,
764 H.: Concentration variation of gaseous and particulate pollutants in the Helsinki city centre—Observations from a two-year
765 campaign from 2013–2015, *Boreal Environ. Res.*, 2019.

766 Timonen, H., Carbone, S., Aurela, M., Saarnio, K., Saarikoski, S., Ng, N. L., Canagaratna, M. R., Kulmala, M., Kerminen, V.-
767 M., Worsnop, D. R., and Hillamo, R.: Characteristics, sources and water-solubility of ambient submicron organic aerosol in
768 springtime in Helsinki, Finland, *J. Aerosol Sci.*, 56, 61-77, <https://doi.org/10.1016/j.jaerosci.2012.06.005>, 2013.

769 Tissari, J.: Fine particle emissions from residential wood combustion (Puun pienpolton pienhiukkaspäästöt), University of
770 Kuopio, Finland, 63 pp., 2008.

771 Todea, A. M., Beckmann, S., Kaminski, H., and Asbach, C.: Accuracy of electrical aerosol sensors measuring lung deposited
772 surface area concentrations, *J. Aerosol Sci.*, 89, 96-109, <https://doi.org/10.1016/j.jaerosci.2015.07.003>, 2015.

773 Tong, X., Ho, J. M. W., Li, Z., Lui, K.-H., Kwok, T. C., Tsoi, K. K., and Ho, K.: Prediction model for air particulate matter
774 levels in the households of elderly individuals in Hong Kong, *Sci. Total Environ.*, 717, 135323,
775 <https://doi.org/10.1016/j.scitotenv.2019.135323>, 2020.

776 Yeh, H.-C., and Schum, G.: Models of human lung airways and their application to inhaled particle deposition, *B. Math. Biol.*,
777 42, 461-480, [https://doi.org/10.1016/S0092-8240\(80\)80060-7](https://doi.org/10.1016/S0092-8240(80)80060-7), 1980.

778 Zaidan, M. A., Wraith, D., Boor, B. E., and Hussein, T.: Bayesian proxy modelling for estimating black carbon concentrations
779 using white-box and black-box models, *Appl. Sci.*, 9, 4976, <https://doi.org/10.3390/app9224976>, 2019.

780 Zaidan, M. A., Motlagh, N. H., Fung, P. L., Lu, D., Timonen, H., Kuula, J., Niemi, J. V., Tarkoma, S., Petäjä, T., Kulmala,
781 M., and Hussein, T.: Intelligent calibration and virtual sensing for integrated low-cost air quality sensors, *IEEE Sens. J.*, 20,
782 13638-13652, 2020.

783 Zhou, Y., Dada, L., Liu, Y., Fu, Y., Kangasluoma, J., Chan, T., Yan, C., Chu, B., Daellenbach, K. R., Bianchi, F., Kokkonen,
784 T. V., Liu, Y., Kujansuu, J., Kerminen, V.-M., Petäjä, T., Wang, L., Jiang, J., and Kulmala, M.: Variation of size-segregated
785 particle number concentrations in wintertime Beijing, *Atmos. Chem. Phys.*, 20, 1201-1216, [https://doi.org/10.5194/acp-20-](https://doi.org/10.5194/acp-20-1201-2020)
786 [1201-2020](https://doi.org/10.5194/acp-20-1201-2020), 2020.

787

788 **Table 1.** Ambient LDSA of alveolar region (in $\mu\text{m}^2 \text{cm}^{-3}$, corrected to 2 significant figures) reported in the last decade in chronological
789 order of the measurement start. TS and RA represent traffic sites and residential area respectively. For the other acronyms, please see the
790 method section.

Site description	Location	Average (Mean, unless state otherwise)	Uncertainties (SD, unless state otherwise)	Period/Season	Instruments	Study
UB	Ruhr, Germany	median=36	IQR=21	Mar 2009–Dec 2014	NSAM	Hennig et al. (2018)
RB+UB+TS	Basel, Geneva, Lugano, Wald, Switerland	32	IQR=25	Jan 2011–Dec 2012	DiSCmini	Eeftens et al. (2016)
City centre with heavy traffic	Lisbon, Portugal	35–89	4–8	Apr–May 2011	NSAM	Albuquerque et al. (2012)
UB	Cassino, Italy	88–240	-	Oct 2011– Mar 2012	NSAM	Buonanno et al. (2012)
RB		69				
UB with traffic influence	Barcelona, Spain	37	26	Nov 2011–May 2013	NSAM	Reche et al. (2015)
TS	Helsinki, Finland	65–94	-	Feb 2012	ELPI,	Kuuluvainen et al. (2016)
RA		15–31			NSAM	
TS	Athens, Greece	65	21 4.8	Jul 2012	Partector Aerotrak 9000	Cheristanidis et al. (2020)
UB with traffic influence	Leicester, UK	30	25	Nov 2013–May 2015	NSAM	Hama et al. (2017)
		23	14	Warm months		
		38	33	Cold months		

Airport	Los Angeles	47	27	Nov–Dec 2014 and May–Jul 2015	DiSCmini	Habre et al. (2018)
UB	Fukuoka, Japan	127	62	Apr 2015–Mar 2016	NSAM	Kiriya et al. (2017)
TS	Helsinki, Finland	60 (ground level) 36-40 (below rooftop) 16-26 (above rooftop)		Nov 2016	Partector, ELPI, DiSCmini, Pegasor AQ Urban	Kuuluvainen et al. (2018)
SC	Helsinki, Finland	22	14	Feb 2017–Jan 2018	Pegasor AQ Urban	Kuula et al. (2020)
UB		9.4	6.9			
DH		12	10			
TS	Delhi, India	330	130	Nov–Dec 2018	ELPI	Salo et al. (2021a)
UB	Salerno	79	48	Nov 2018– May 2019	NanoTracer	Pacitto et al. (2020)
TS	Roma, Italy	110	57			
RB	Parma, Italy	17	10			

791

792

793

794 **Table 2.** Descriptive statistics of alveolar LDSA concentrations ($\mu\text{m}^2 \text{cm}^{-3}$) at SC (2017–2018), UB (2017–May 2018), DH1–3 (2018) and
795 RB (2018) site. The mean (column 3), standard deviation (SD, column 4), 10th, 25th, 50th, 75th and 90th percentile (P10, P25, P50, P75 and
796 P90, column 5–9), geometric mean (Gmean, column 10) and geometric standard deviation (GSD, column 11) of the concentrations are
797 corrected to one decimal place. The percentage of valid data in the reported measurement period is shown in column 12.

		Mean	SD	P10	P25	P50	P75	P90	Gmean	GSD	%
SC	All	19.7	11.3	8.4	11.7	17.0	24.7	34.4	17.0	1.7	97
	Winter	19.4	12.2	7.6	10.7	16.1	24.7	35.3	16.3	1.8	98
	Spring	19.6	11.0	8.6	11.8	16.9	24.3	34.2	17.1	1.7	94
	Summer	20.8	10.4	10.5	13.5	18.4	25.5	34.2	18.6	1.6	98
	Autumn	18.4	11.7	7.1	10.0	15.0	23.8	34.6	15.3	1.8	96
	Workdays	21.4	12.3	8.6	12.5	18.8	27.7	37.6	18.4	1.8	97
	Weekends	15.9	7.5	8.1	10.7	14.4	19.4	25.2	14.4	1.6	97
UB	All	11.2	7.1	4.6	6.4	9.5	14.0	19.6	9.5	1.8	70
	Winter	12.4	9.1	4.8	6.3	10.0	15.4	22.5	10.1	1.9	89
	Spring	10.4	6.1	4.6	6.2	9.0	12.8	18.3	9.0	1.7	100
	Summer	12.8	5.8	6.7	8.5	11.4	15.8	20.7	11.6	1.6	57
	Autumn	7.7	4.7	3.2	4.5	6.7	9.7	13.2	6.7	1.7	56
	Workdays	11.5	7.3	4.8	6.7	9.7	14.1	20.3	9.8	1.8	70
	Weekends	10.4	6.6	4.1	5.8	8.8	13.6	18.3	8.8	1.8	70
DH1–3	All	11.7	8.6	4.2	6.3	9.7	14.5	21.1	9.5	1.9	94
	Winter	12.3	10.2	4.1	6.2	9.6	14.8	23.4	9.7	2.0	86
	Spring	12.8	8.2	5.3	7.4	10.8	15.9	23.1	10.7	1.8	98
	Summer	11.8	5.9	5.7	7.8	10.8	14.5	19.2	10.6	1.6	98
	Autumn	10.5	10.2	3.0	4.6	6.8	13.0	22.2	7.5	2.2	95
	Workdays	11.8	8.3	4.3	6.4	9.9	14.6	20.8	9.6	1.9	95
	Weekends	11.7	9.3	4.0	6.0	9.4	14.3	21.8	9.3	2.0	93
RB	All	7.6	5.4	2.4	4.0	6.5	10.2	14.0	6.1	2.0	99
	Winter	6.6	6.0	2.2	3.5	5.6	8.3	11.6	5.3	1.9	100
	Spring	9.1	6.4	3.5	5.1	7.4	11.0	16.6	7.5	1.9	99
	Summer	9.8	4.3	4.7	6.6	9.3	12.5	15.3	8.9	1.6	99
	Autumn	4.9	4.1	1.6	2.6	3.9	5.6	8.9	3.8	2.0	99
	Workdays	7.7	5.6	2.5	4.1	6.6	10.2	14.1	6.2	2.0	99
	Weekends	7.6	5.0	2.4	4.0	6.5	10.1	14.0	6.1	2.0	100

798

799

800

801 **Table 3.** The evaluation attributes by IAME model at the SC and the UB site, corrected to 2 significant figures.

	Street canyon					Urban background				
	R^2	MAE	$cRMSD$	r	NSD	R^2	MAE	$cRMSD$	r	NSD
All	0.80	3.7	5.6	0.87	0.78	0.77	2.3	3.7	0.86	0.80
Winter	0.86	3.4	5.3	0.92	0.74	0.81	2.5	4.6	0.89	0.68
Spring	0.75	3.9	5.9	0.85	0.79	0.61	2.4	3.3	0.84	0.85
Summer	0.70	4.1	5.9	0.83	0.84	0.61	2.7	3.7	0.79	0.95
Autumn	0.85	3.4	5.4	0.9	0.75	0.85	1.3	2.0	0.91	0.83
Workdays	0.81	4.1	6.1	0.87	0.77	0.75	2.4	3.8	0.86	0.77
Weekends	0.72	3.0	4.3	0.82	0.82	0.8	2.1	3.5	0.85	0.87

802

803

804 **Table 4.** Five most successful sub-models at the SC site. The table shows only the fixed predictors with their coefficient (β , all $p < 0.05$) and
805 corresponding standard error (SE). The variance inflation factor (VIF) among the fixed predictors is also shown for the 5 sub-models. The
806 evaluation attributes of the sub-models are shown column 6–10. The percentage of the sub-model usage and the number of data points (n)
807 is shown in column 11 and 12. Natural logarithm is taken for parameters with asterisk (*).

	Fixed predictors	β	SE	VIF	R^2	MAE	cRMSD	r	NSD	%	n
1	*PM _{2.5}	0.119	0.005	1.54							
	*PNC	0.313	0.005	2.89	0.74	3.7	5.7	0.87	0.79	81	2603
	*BC	0.223	0.004	2.17							
2	*NO _x	0.236	0.005	3.79							
	*PNC	0.153	0.005	1.63	0.74	3.8	5.7	0.86	0.77	13	2629
	*BC	0.231	0.007	4.90							
3	*PNC	-0.044	0.003	1.07							
	*BC	0.375	0.004	2.20	0.74	3.8	5.8	0.86	0.78	4	6622
	WS	0.201	0.004	2.15							
4	*NO _x	0.250	0.005	3.09							
	*PM _{2.5}	0.243	0.004	1.17	0.74	3.8	5.7	0.87	0.78	<1	2596
	*PNC	0.184	0.005	3.02							
5	*NO _x	0.176	0.005	3.51							
	*PM ₁₀	0.070	0.004	1.3	0.72	3.8	5.8	0.85	0.75	<1	2713
	*BC	0.326	0.006	3.65							

808

809

810 **Table 5.** Five most successful sub-models at the UB site. The table shows only the fixed predictors with their coefficient (β , all $p < 0.05$) and
811 corresponding standard error (SE). The variance inflation factor (VIF) among the fixed predictors is also shown for the 5 sub-models. The
812 evaluation attributes of the sub-models are shown column 6–10, corrected to 2 significant figures. The percentage of the sub-model usage
813 and the number of data points (n) is shown in column 11 and 12. Natural logarithm is taken for parameters with asterisk (*).

	Fixed predictors	β	SE	VIF	R^2	MAE	cRMSD	r	NSD	%	n
1	*CO	0.072	0.027	1.72							
	*PNC	0.400	0.006	2.08	0.84	1.7	2.5	0.92	0.87	49	941
	*BC	2.956	0.007	1.52							
2	*PNC	-0.098	0.005	1.09							
	*BC	0.398	0.004	1.44	0.82	1.9	2.9	0.91	0.89	17	6608
	WD-N	0.328	0.006	1.55							
3	*NO ₂	0.237	0.007	1.88							
	*CO	0.520	0.024	1.10	0.69	2.4	3.4	0.84	0.73	17	941
	*PNC	0.341	0.010	2.00							
4	*CO	0.009	0.000	1.08							
	*PNC	0.348	0.025	1.07	0.58	2.7	3.9	0.77	0.63	11	9757
	RH	0.590	0.007	1.15							
5	*NO _x	0.107	0.006	2.22							
	*CO	0.182	0.032	1.72	0.81	1.9	3.0	0.90	0.85	2	7036
	*BC	0.455	0.007	2.56							

814

815

816

817

818 **Table 6.** Model evaluation comparison of deposition model derived LDSA (LDSA_{ICRP}), modelled LDSA by IAP (LDSA_{IAP}) and modelled
819 LDSA by IAME (LDSA_{IAME}) against reference measurements LDSA_{Pegasor} at the SC and the UB site. Parameters with an asterisk represent
820 natural logarithm. The evaluation attributes of the three methods are corrected to 2 significant figures.

	Street canyon					Urban background				
	R^2	MAE	$cRMSD$	r	NSD	R^2	MAE	$cRMSD$	r	NSD
LDSA _{ICRP}	0.72	4.1	6.2	0.88	1.1	0.83	1.8	2.9	0.93	1.1
LDSA _{IAP}	0.77	4.0	6.0	0.85	0.78	0.66	2.8	3.9	0.84	0.81
LDSA _{IAME}	0.80	3.7	5.6	0.87	0.78	0.77	2.3	3.7	0.86	0.80

821

822

823 **Table 7.** Statistics to show temporal difference. The number of data (n), mean and standard deviation (SD) of absolute error and the
 824 corresponding *p*-values of t-tests at the selected time windows at both sites.

Street canyon (SC)	n	Mean	SD	t-test	<i>p</i>
Workdays	11658	4.1	4.8	Workdays vs Weekends	4.13×10^{-81}
Weekends	5322	3.0	3.2		
				Winter vs Spring	3.64×10^{-24}
Winter	4023	3.4	4.2	Winter vs Summer	5.89×10^{-5}
Spring	2297	4.0	4.5	Winter vs Autumn	7.07×10^{-7}
Summer	6457	4.2	4.4	Spring vs Summer	6.38×10^{-34}
Autumn	4320	3.4	4.3	Spring vs Autumn	1.02×10^{-4}
				Summer vs Autumn	2.69×10^{-15}
Hour 4–10 a.m.	4953	4.8	5.6	Hour 4–10 a.m. vs 4–10 p.m.	2.58×10^{-40}
Hour 4–10 p.m.	4981	3.5	3.6		
Urban background (UB)	n	Mean	SD	t-test	<i>p</i>
Workdays	8473	2.3	2.6	Workdays vs Weekends	5.08×10^{-8}
Weekends	3852	2.1	2.6		
				Winter vs Spring	1.96×10^{-7}
Winter	2539	2.5	3.2	Winter vs Summer	0.39***
Spring	1101	1.9	3.1	Winter vs Autumn	1.90×10^{-2}
Summer	1628	2.6	2.4	Spring vs Summer	2.75×10^{-9}
Autumn	812	2.3	2.1	Spring vs Autumn	2.20×10^{-3}
				Summer vs Autumn	1.40×10^{-3}
Hour 4–10 a.m.	3620	2.3	2.7	Hour 4–10 a.m. vs 4–10 p.m.	0.86***
Hour 4–10 p.m.	3591	2.3	2.7		
	n	Mean	SD	t-test	<i>p</i>
Street canyon (SC)	11940	3.9	4.6	SC vs UB (in same time period)	8.21×10^{-246}
Urban background (UB)		2.3	2.6		

825

826

827 *** $p > 0.05$ the null hypothesis of different distribution is rejected

828

829

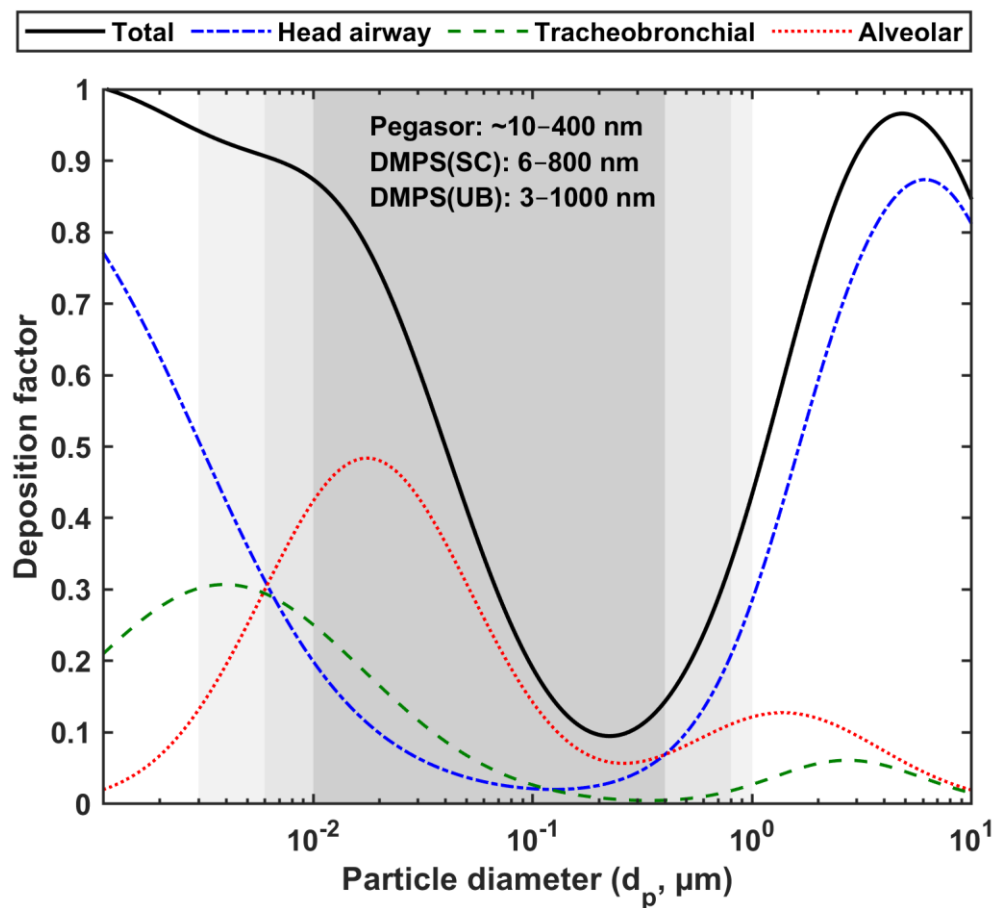


Figure 1. Lung deposition factor of a spectrum of particle size distribution based on the equation (ICRP, 1994). Black solid line represents the total deposition factor while blue, green and red dotted line refer to deposition factor in head airway, tracheobronchial and alveolar region, respectively. Pegasor AQ Urban measured the alveolar LDSA concentration of particles in the $\sim 10\text{--}400$ nm size range (dark grey). DMPS at SC and UB were used to calculate alveolar LDSA in selected size fractions in the $6\text{--}800$ nm and $3\text{--}1000$ nm size range, respectively.

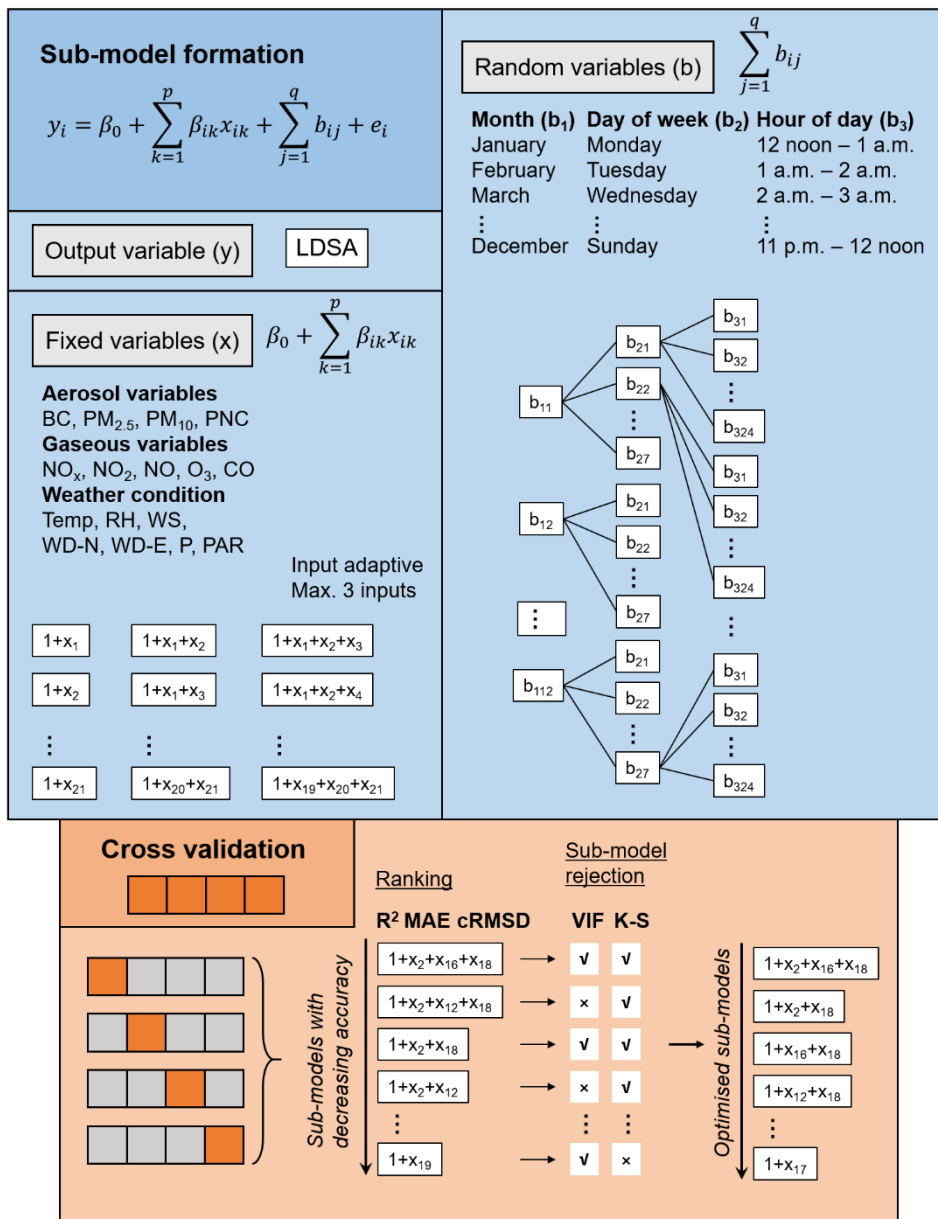
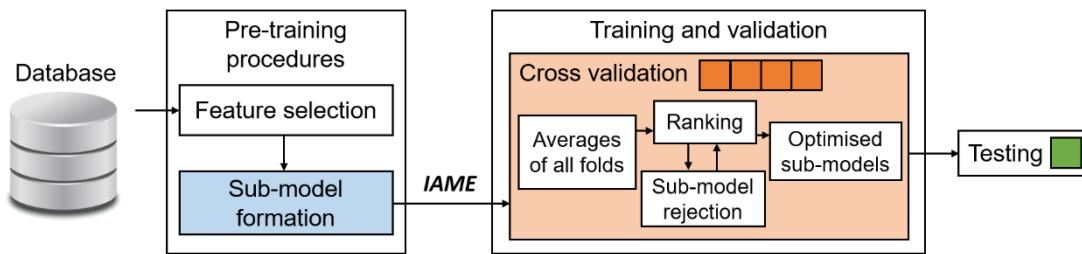


Figure 2. The block diagram of the proxy procedures (top). The blue and orange blocks are explanatory notes to the sections of sub-model formation and cross validation, respectively.

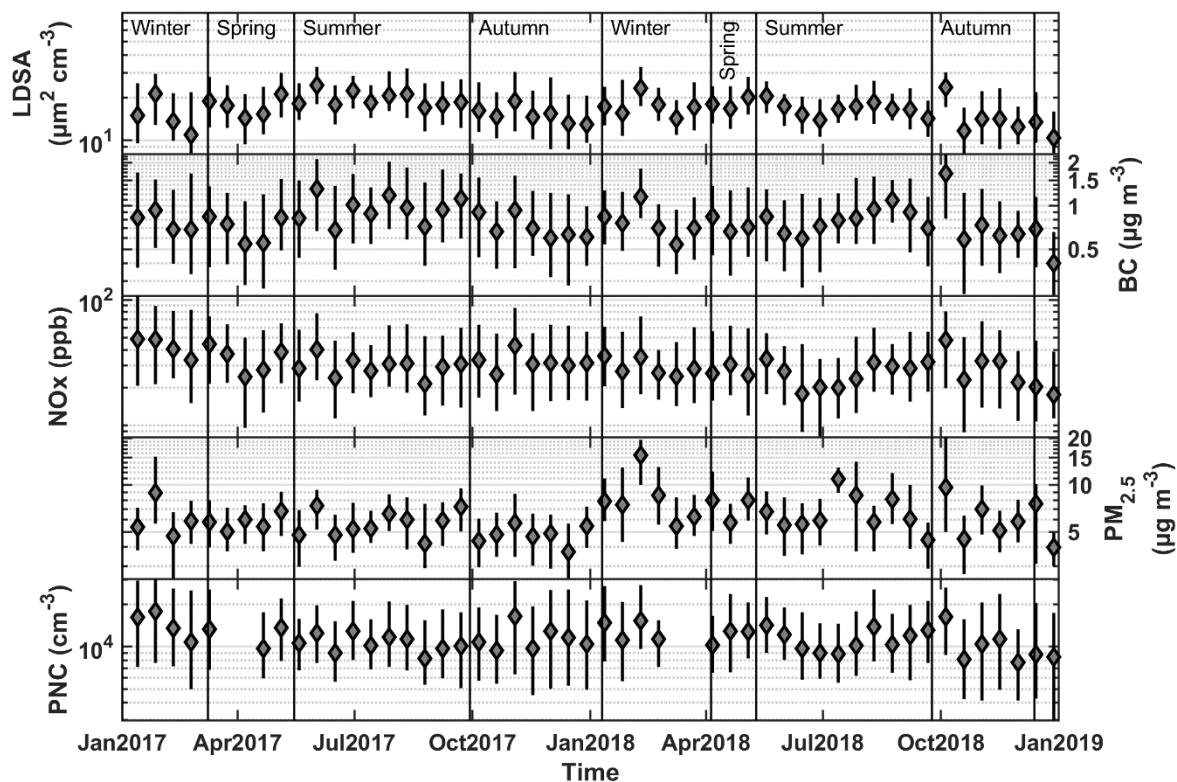


Figure 3. Time series of the selected air pollutant parameters (First to end row: LDSA ($\mu\text{m}^2 \text{cm}^{-3}$), BC ($\mu\text{g m}^{-3}$), NO_x (ppb), PM_{2.5} ($\mu\text{g m}^{-3}$) and PNC (cm^{-3})) at Mäkelänkatu SC site during the measurement period from 1 January 2017 and 31 December 2018. Each bar represents a period of two weeks where the shaded diamond marker is the median and the vertical error bars are the 25th and 75th percentiles. Seasons are thermally separated.

832

833

834

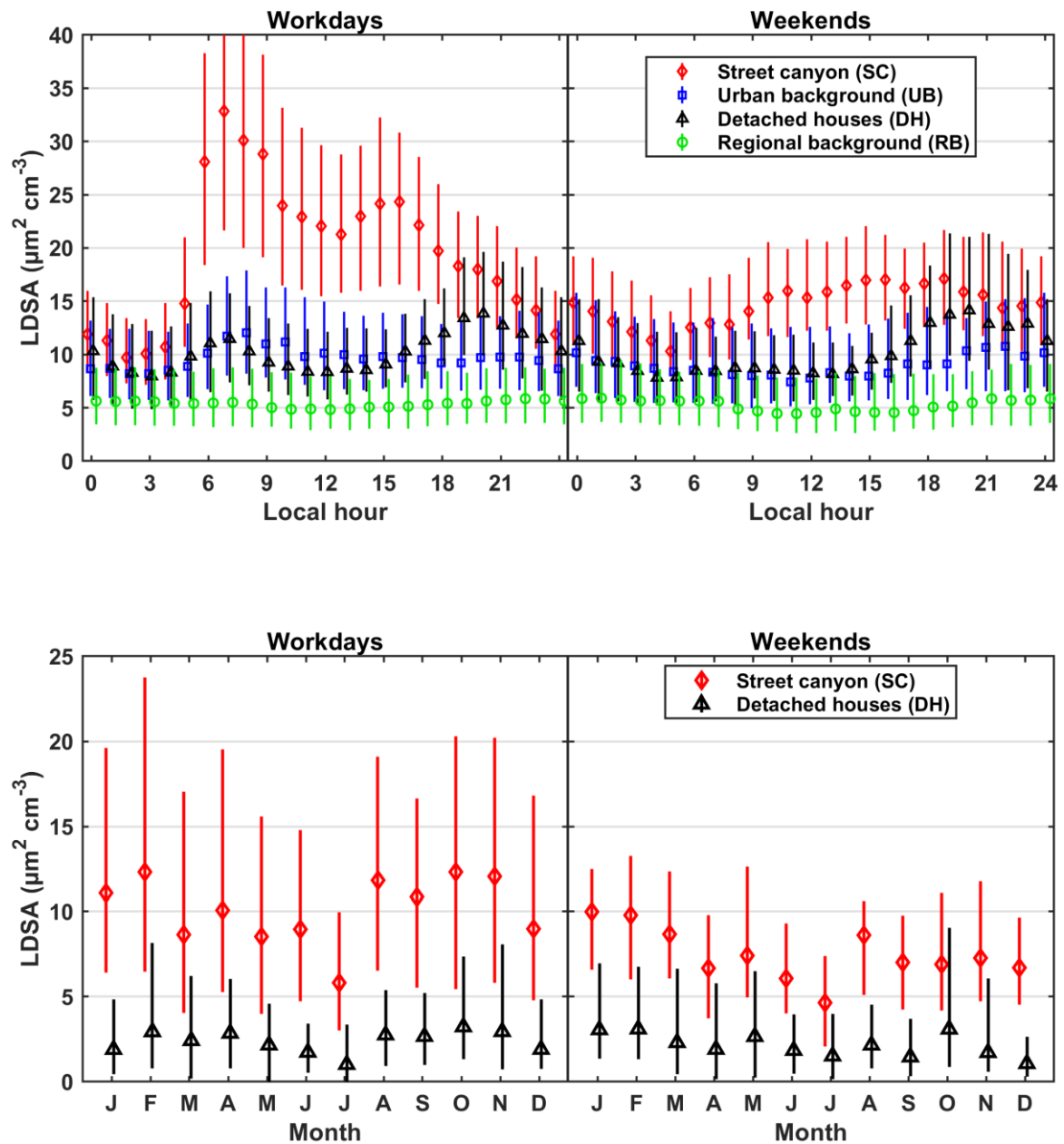


Figure 4. Upper panel: Diurnal cycles of LDSA concentrations ($\mu\text{m}^2 \text{cm}^{-3}$) at SC (red diamond, 2017–2018), UB (blue square, 2017–May 2018), DH1–3 (black triangle, 2018) and RB site (green circle, 2018) on workdays and weekends with error bars of 25th and 75th percentiles. Lower panel: Monthly averages in year 2018 of local LDSA increments at the SC (red diamond) and DH1–3 (black triangle) site (LDSA concentration at the hotspot site – LDSA at RB site) on workdays and weekends with error bars of 25th and 75th percentiles.

835

836

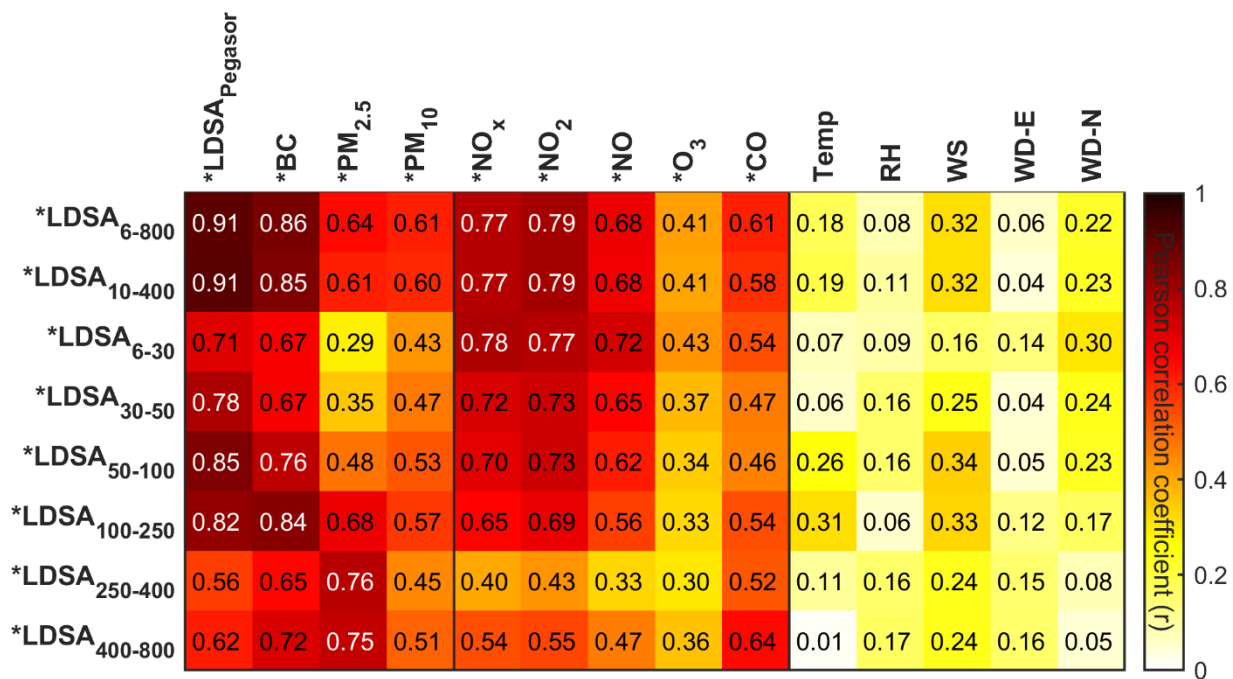


Figure 5. Heatmap showing Pearson correlation coefficient (r , corrected to 2 significant figures) of LDSA of different particle size sections (in nm) by ICRP lung deposition model and the other air pollutant parameters at Mäkelänkatu SC site. Dark red indicates a high correlation while pale yellow indicates a low correlation. Parameters with an asterisk represent natural logarithm. LDSA_{Pegasor} represents the measured LDSA concentrations.

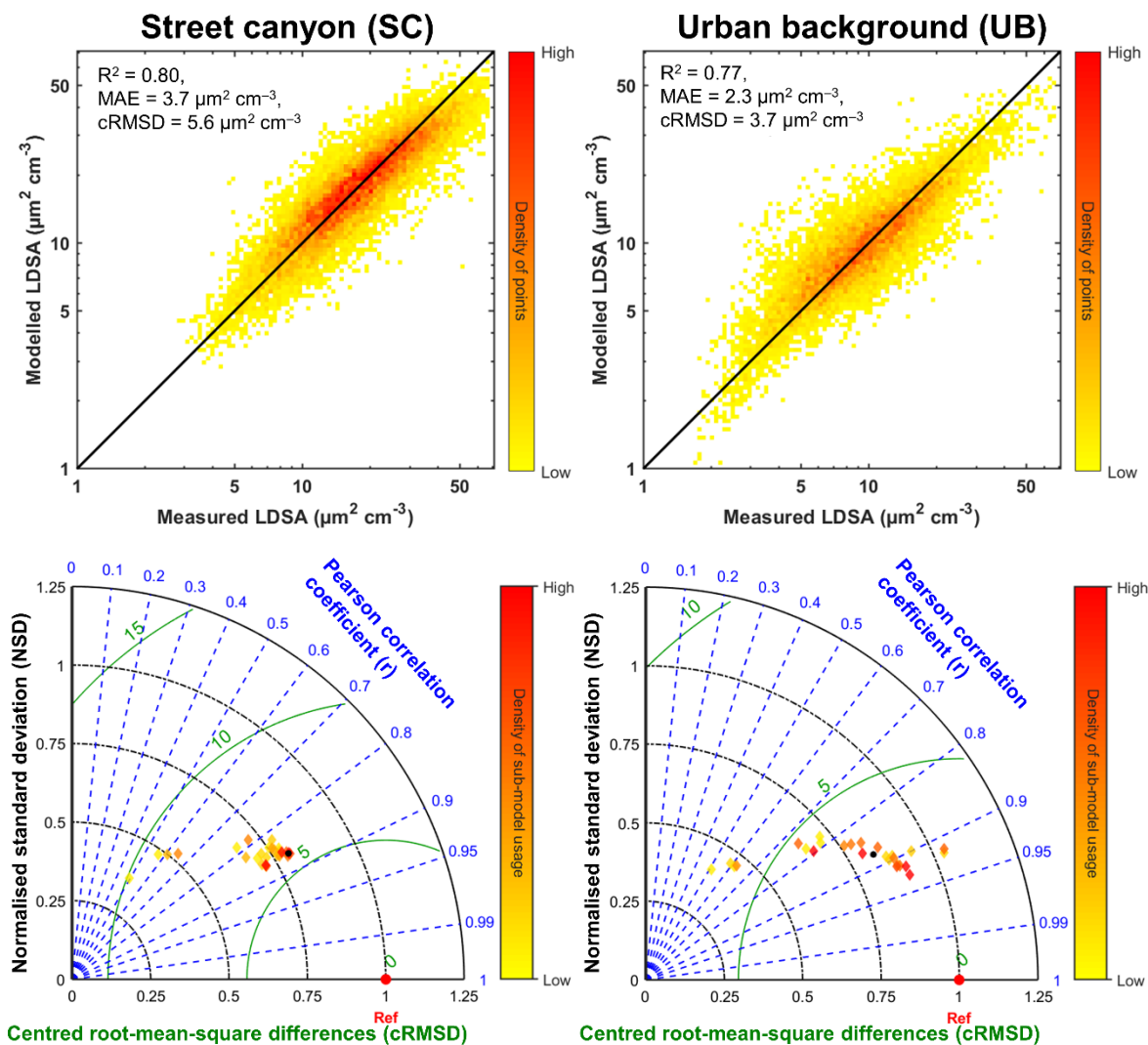


Figure 6. The upper panel shows the Taylor's diagrams (Taylor, 2001) at Mäkeläkatu SC site (first column) and at Kumpula UB site (second column). Each diamond marker in the Taylor's diagrams represents each sub-model used in the final estimation by IAME (solid black dot), compared with the reference data (solid red dot). Hues of colours represent how frequent the sub-model was used. The upper panel shows the scatter plots of modelled LDSA against the measured LDSA at Mäkeläkatu SC site (first column) and at Kumpula UB site (second column). Hues of colours represent the density of points on the figure. The lower panel shows the Taylor's diagrams (Taylor, 2001) at Mäkeläkatu SC site (first column) and at Kumpula UB site (second column). Each diamond marker in the Taylor's diagrams represents each sub-model used in the final estimation by IAME (solid black dot), compared with the reference data (solid red dot). Hues of colours represent how frequent the sub-model was used.

838

839

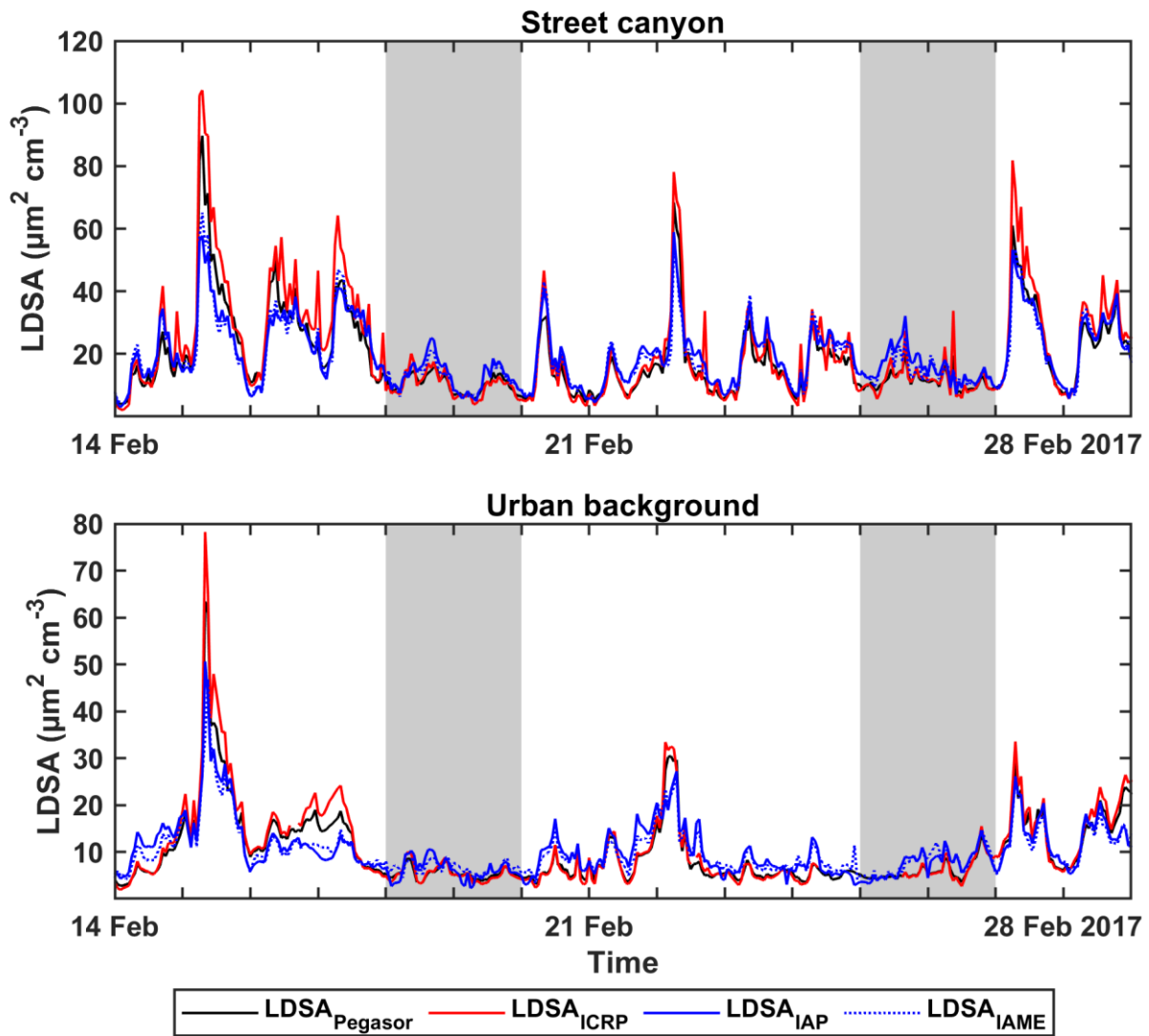


Figure 7. Timeseries of measured LDSA ($LDSA_{Pegasor}$, black), deposition model derived LDSA by ICRP ($LDSA_{ICRP}$, red), modelled LDSA by IAP ($LDSA_{IAP}$, blue solid line) and modelled LDSA by IAME ($LDSA_{IAME}$, blue dotted line) during a selected measurement window between 14 and 28 February 2017. Shaded regions represent weekends, otherwise workdays.

840

841

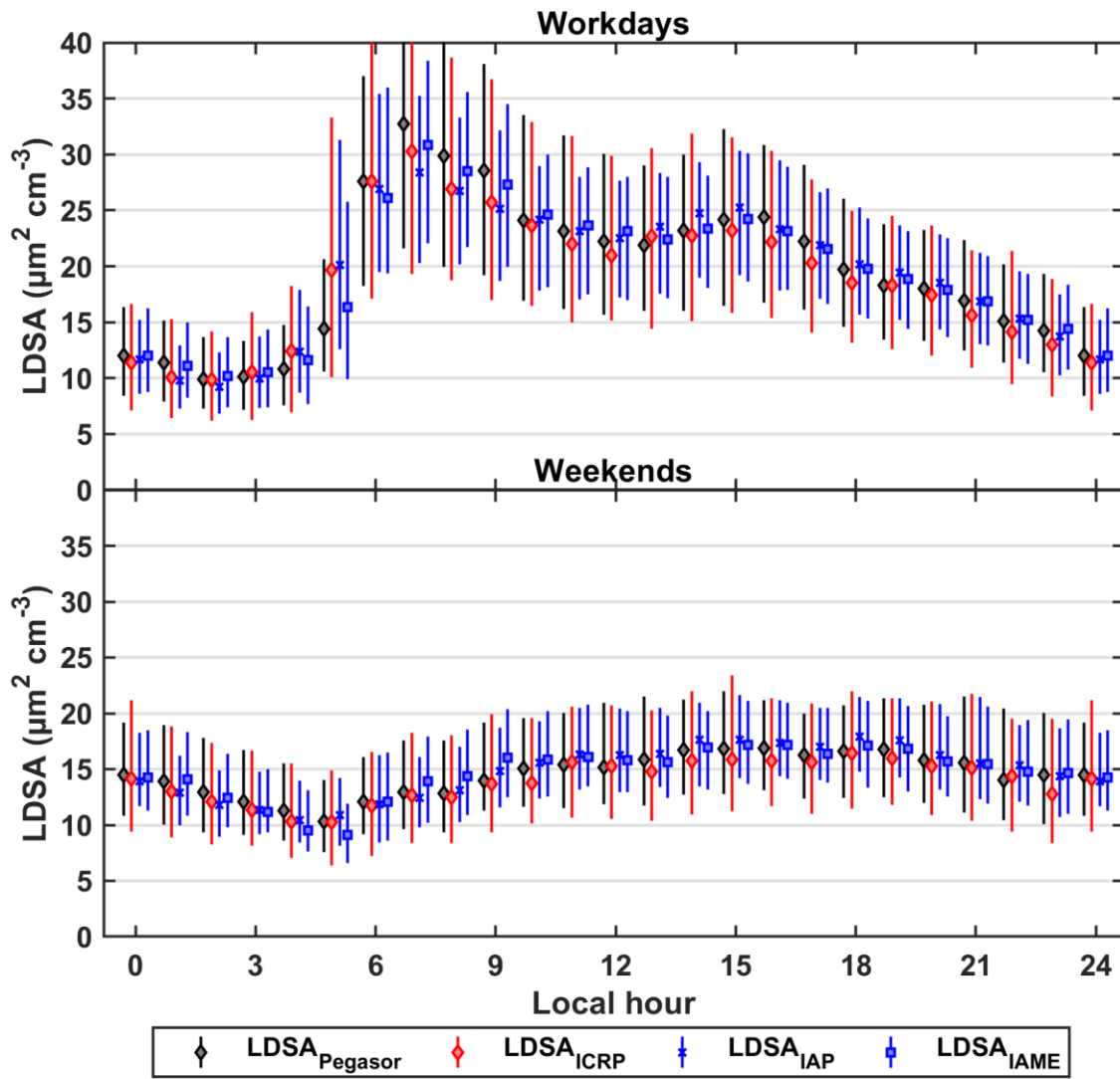


Figure 8. Diurnal cycles of measured ($LDSA_{Pegasor}$, black), deposition model derived ($LDSA_{ICRP}$, red) and modelled ($LDSA_{IAP}$ and $LDSA_{IAME}$, blue) LDSA concentrations with error bars of 25th and 75th percentiles on workdays (left) and weekends (right). $LDSA_{IAP}$ and $LDSA_{IAME}$ can be differentiated by their markers, cross for the former and square for the latter.

842

843